ORNL/TM-2016/680

Oak Ridge National Laboratory Simulations of a “PSD Plastic” Neutron Collar for Assaying Fresh Fuel

Approved for public release.
Distribution is unlimited.

Paul Hausladen
Jason Newby
Bob McElroy

November 2016

OAK RIDGE NATIONAL LABORATORY
MANAGED BY UT-BATTELLE FOR THE US DEPARTMENT OF ENERGY

DOCUMENT AVAILABILITY

Reports produced after January 1, 1996, are generally available free via US Department of Energy (DOE) SciTech Connect.

Website http://www.osti.gov/scitech/

Reports produced before January 1, 1996, may be purchased by members of the public from the following source:

National Technical Information Service
5285 Port Royal Road
Springfield, VA 22161
Telephone 703-605-6000 (1-800-553-6847)
TDD 703-487-4639
Fax 703-605-6900
E-mail info@ntis.gov
Website http://www.ntis.gov/help/ordermethods.aspx

Reports are available to DOE employees, DOE contractors, Energy Technology Data Exchange representatives, and International Nuclear Information System representatives from the following source:

Office of Scientific and Technical Information
PO Box 62
Oak Ridge, TN 37831
Telephone 865-576-8401
Fax 865-576-5728
E-mail reports@osti.gov
Website http://www.osti.gov/contact.html

This report was prepared as an account of work sponsored by an agency of the United States Government. Neither the United States Government nor any agency thereof, nor any of their employees, makes any warranty, express or implied, or assumes any legal liability or responsibility for the accuracy, completeness, or usefulness of any information, apparatus, product, or process disclosed, or represents that its use would not infringe privately owned rights. Reference herein to any specific commercial product, process, or service by trade name, trademark, manufacturer, or otherwise, does not necessarily constitute or imply its endorsement, recommendation, or favoring by the United States Government or any agency thereof. The views and opinions of authors expressed herein do not necessarily state or reflect those of the United States Government or any agency thereof.

ORNL/TM-2016/680

Nuclear Security and Isotope Technology Division

SIMULATIONS OF A "PSD PLASTIC" NEUTRON COLLAR FOR ASSAYING FRESH FUEL

Paul Hausladen
Jason Newby
Bob McElroy

Date Published: November 2016

Prepared by
OAK RIDGE NATIONAL LABORATORY
Oak Ridge, TN 37831-6283
managed by
UT-BATTELLE, LLC
for the
US DEPARTMENT OF ENERGY
under contract DE-AC05-00OR22725

CONTENTS

LIST OF FIGURES

LIST OF TABLES

ACRONYMS AND ABBREVIATIONS

IAEA	International Atomic Energy Agency
LEU	low-enriched uranium
MCNP	Monte Carlo N-Particle
ORNL	Oak Ridge National Laboratory
PMT	photomultiplier tube
PSD	pulse shape discrimination
PUNCL	PSD-Plastic UNCL
SiPM	silicon photomultiplier
UNCL	Uranium Neutron Coincidence Collar for LEU

ABSTRACT

The potential performance of a notional active coincidence collar for assaying uranium fuel based on segmented detectors constructed from the new “PSD plastic” fast organic scintillator with pulse shape discrimination capability was investigated in simulation. Like the International Atomic Energy Agency’s present Uranium Neutron Coincidence Collar for LEU (UNCL), the PSD plastic collar would also function by stimulating fission in the ^{235}U content of the fuel with a moderated ^{241}Am/Li neutron source and detecting instances of induced fission via neutron coincidence counting. In contrast to the moderated detectors of the UNCL, the fast time scale of detection in the scintillator eliminates statistical errors due to accidental coincidences that limit the performance of the UNCL. However, the potential to detect a single neutron multiple times historically has been one of the properties of organic scintillator detectors that has prevented their adoption for international safeguards applications. Consequently, as part of the analysis of simulated data, a method was developed by which true neutron-neutron coincidences can be distinguished from inter-detector scatter that takes advantage of the position and timing resolution of segmented detectors. Then, the performance of the notional simulated coincidence collar was evaluated for assaying a variety of fresh fuels, including some containing burnable poisons and partial defects. In these simulations, particular attention was paid to the analysis of “fast mode” measurements. In fast mode, a Cd liner is placed inside the collar to shield the fuel from the interrogating source and detector moderators, thereby eliminating the thermal neutron flux that is most sensitive to the presence of burnable poisons that are ubiquitous in modern nuclear fuels. The simulations indicate that the predicted precision of “fast mode” measurements is similar to what can be achieved by the present UNCL in thermal mode. For example, the statistical accuracy of a ten-minute measurement of fission coincidences collected in “fast mode” will be approximately 1% for most fuels of interest, yielding an ~1.4% error after subtraction of a five-minute measurement of the spontaneous fissions from ^{238}U in the fuel, an ~2% error in analyzed linear density after accounting for the slope of the calibration curve, and an ~2.9% total error after addition of an assumed systematic error of 2%.

1. INTRODUCTION

The present work is part of a comparative study supported by NA-241’s Safeguards Technology group to evaluate several commercially available detector material alternatives to moderated ^{3}He proportional counters for quantifying fissile uranium in fresh fuel. The International Atomic Energy Agency (IAEA) currently uses the uranium neutron coincidence collar (UNCL) for this application [1, 2].

The UNCL consists of a moderated ^{241}Am/Li neutron source and detector that fit around a fuel assembly, with the source moderator on one side and three neutron detector banks on the three remaining sides. Neutrons from the ^{241}Am/Li source stimulate fission in the ^{235}U content of the fuel, and instances of induced fission are detected via neutron coincidence counting. The coincidence counting separates the fission neutrons from the random neutrons used in the interrogation. Almost all of the ^{241}Am/Li neutrons are sufficiently low in energy (below the ~1-MeV fission barrier in ^{238}U) so that the primary fission rate in ^{238}U is negligible.

Modern uranium fuels use burnable poisons to achieve high burnup through the use of higher enrichments. To this end, fuel designers include burnable poisons (such as Gd) into fuel assemblies to control the additional reactivity of fresh fuel assemblies. The addition of burnable poisons makes fissile uranium assay more difficult using the UNCL. In particular, for fuels with burnable poisons, the removal of interrogating neutrons by neutron capture in the poison lowers the induced fission rate. Correction for the presence of burnable poison depends on operator-declared information regarding the linear density of burnable poison, and for higher burnable poison loadings, this correction can be by as large as a factor of two in analyzed mass. To reduce the dependence of the induced fission rate on burnable poisons, the UNCL can be used in fast mode. In fast mode, a Cd liner is placed inside the UNCL to shield the fuel from the source and detector moderators, thereby eliminating the thermal neutron flux that is modified by the presence of burnable poison. As a result, the sensitivity of the measurement to the presence of burnable poisons is drastically reduced.

Due to the long coincidence times (64 μs) and high rates, the precision of the UNCL is limited primarily by the accidental coincidence rate. This is particularly true in fast mode, where elimination of the thermal neutrons by the Cd liner reduces the induced-fission rate by about an order of magnitude while the background accidental coincidence rate, originating largely from the interrogation source neutrons, is only marginally reduced. As a result, measurement times to reach adequate statistical precision in fast mode are substantially longer, on the order of an hour.

Scintillation-based fast neutron detectors are a potentially superior technology to existing coincidence counter designs because their inherently short neutron coincidence times essentially eliminate random coincidences. In contrast to moderated detectors, where neutron detection times are determined by moderation times (typically tens of microseconds), detection times of fission neutrons in proton-recoil scintillators are determined by neutron times of flight from the fission site (typically tens of nanoseconds). This prompt detection time allows the coincidence window and therefore the accidental coincidence rate to be reduced by three orders of magnitude. Moreover, the typical ~1-MeV threshold in these scintillators reduces their sensitivity to ^{241}Am/Li source neutrons in comparison to fission neutrons, resulting in another order of magnitude reduction in the random coincidence rate. The combination of these two factors makes the accidental coincidence rate insignificant.

There are a number of fast organic scintillator materials that detect neutrons via proton recoil and can distinguish neutron interactions from gamma-ray interactions via pulse shape discrimination (PSD). The most common of these are liquid scintillators (such as EJ-309), but recently, large, single-crystal stilbene has become available [3], as has plastic scintillator with PSD capability [4], which we refer to colloquially as "PSD plastic." Historically, a number of properties of organic scintillator detectors have prevented their adoption for international safeguards applications, including the potential to detect a single neutron multiple times, sensitivity to gamma rays, and the need for comparatively complicated data acquisition and analysis. At present, it is appropriate to reassess the potential value of using fast scintillators for the purpose of coincidence counting because:

- The recent availability of PSD plastic detectors that are mechanically robust and solid form has obvious benefits compared to liquid scintillator and fragile organic crystals;
- Complicated data acquisition and analysis for pulse-shape discrimination is becoming manageable using off-the-shelf waveform digitizers combined with appropriate software; and
- Recent observation indicates that empirically, multiple-scatter coincidences group at a characteristic apparent scatter velocity, v_s, between detection positions, enabling the scatter contribution to the coincidence time distribution to be distinguished from fission.

Recently, Oak Ridge National Laboratory (ORNL) evaluated a set of segmented detectors constructed from commercially available PSD plastic for the purpose of fast-neutron coincidence counting [5]. These detectors were originally built to instrument the focal plane of a fast-neutron imager, but the position and time resolution permitted by segmented detectors enabled separation of fission coincidences from inter-detector scattering using the kinematics of neutron scattering. The results were sufficiently encouraging to motivate this simulation study for the purpose of evaluating the potential of similarly segmented PSD plastic detectors for quantifying fissile uranium in fresh fuel. This document reports results from that simulation study. This work addresses the IAEA Department of Safeguards Long-Term R&D Plan, 2012-2023, need 5.8: "Develop alternative NDA instruments, for instance based on liquid scintillators, to improve performance in neutron coincidence counting techniques applied to various types of fissile material."

The remainder of this document is organized as follows: First, the components and geometry of the simulated PSD-Plastic UNCL (PUNCL) will be described. Then, the simulation methodology, quantities recorded, and data analysis to infer the number of fissions from measurements will be described. Following these descriptions, the results of simulated calibrations to relate the rate of detected neutron coincidences to the linear density of ^{235}U will be reported. Finally, the performance of the notional simulated PUNCL will be evaluated for assaying a variety of fresh fuels, including some containing burnable poisons and partial defects.

2. THE “PSD PLASTIC” COLLAR

For the purposes of this simulation study, the philosophy of the notional design for the PSD plastic collar was to echo the present design of the UNCL while using detectors that were representative of the present ORNL segmented PSD plastic detectors. In this way, the study was intended to primarily provide information regarding the safeguards utility of fast proton-recoil scintillator, segmented detectors, and the ability to identify and eliminate inter-detector scattering. For instance, no significant effort was spent tweaking the geometry or constituents of the moderator to modify the interrogating neutron flux or spectrum. As a result, the instrument was modeled as a four-sided system similar to the UNCL with three sides of detectors and one side consisting of a moderated ^{241}Am/Li source identical to that used in the UNCL. In the fast-mode, the fuel was surrounded by a 1-mm layer of cadmium extending 340 mm along the length of the fuel. Vertically centered about the cadmium liner were 12 PSD plastic volumes, each 12 × 12 cm on a face with a depth of 5 cm arranged in a 2 × 2 array on each of three sides. In each corner, a block of plastic was used as passive shielding to limit multiple scattering of neutrons between adjacent sides. A cross-sectional view of the (right) PSD-plastic collar and the (left) UNCL are shown in Fig. 1. Additional inactive volumes, such as light guides, light readout [photomultiplier tubes or silicon photomultipliers (PMTs or SiPMs)], detector housings, and electronics were not included in the simulation.

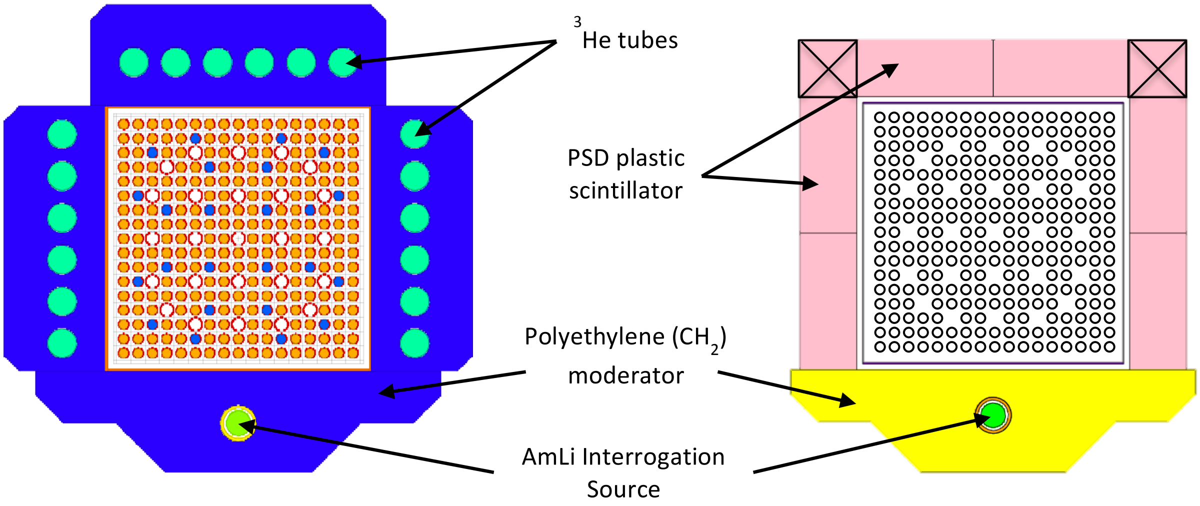

Fig. 1. Schematic diagram of (left) the UNCL and (right) the PSD plastic collar. Six of twelve detectors are visible for the PSD plastic collar, the other six being beneath those shown. The blocks marked with an ‘X’ indicate the location of the plastic passive shielding.

2.1 SIMULATIONS

Simulations were performed using Monte Carlo N-Particle (MCNP) 6.1.1b coupled with a locally authored detector response and coincidence analysis that used the MCNP6 “ptrac” stream. In the simulations, the Lawrence Livermore National Laboratory fission model was specified using the FMULT card via (e.g.) `FMULT 92235 METHOD=5` [6]. To ensure that each run had a unique seed, random number seeds were dumped from the `/dev/random` pseudorandom number generator as unsigned decimals via the octal dump utility and printed to the input file via the command:

```
od -N7 -tu /dev/random | head -1 | awk
{a=($3*2^32+$2);if(a%2==0){a+=1;};print a;}'
```

Use of different seeds removed correlations that were apparent in separate simulations of similar fuel configurations. The MCNP particle tracking (PTRAC) binary-formatted output was directed to a named pipe via the command:

```
PTRAC BUFFER=100 FILE=BOV WRITE=ALL EVENT=SRC,COL,SUR,BNK,TER
MAX=4611686018427387904
```

All particle interactions (proton elastic scattering, fission, etc.) and surface crossings were streamed to the pipe, which was parsed and analyzed by a user-developed executable called ptracToROOT. For each MCNP history, the executable identified a set of particle surface crossings into each of the detector volumes and associated with each surface event all energy depositions (proton recoil, Compton scattering, etc.) before the particle exited the volume or terminated.

For the above data, two separate analyses were performed. In one instance, the “ideal” or “per particle” analysis was performed. In the other instance, the “realistic” or “coincidence summed” analysis was performed. The ideal analysis treated each particle separately. For each particle, the interactions were time sorted and the first interaction depositing greater than 5 keV set both the time and the particle ID of the detector hit. The remaining interactions were processed to determine the total energy deposition and an energy-weighted three-dimensional position. The present simulations did not include scintillator light yields. Instead, light yields were approximately accounted for by requiring a total energy deposition of 750 keV to identify a neutron. In contrast, the coincidence-summed analysis treated each detector separately, and reflects the limitations of the digital signal processing of the current electronics that do not distinguish multiple simultaneous interactions within the same detector volume within about 2 μs. For this coincidence-summed case, all interactions within the same volume are processed to produce a single observable detector hit. As before, the interactions were time sorted, and the first interaction depositing greater than 5 keV set both the time and the particle ID of the observed hit, and the remaining interactions processed to determine the total energy deposition and energy-weighted three-dimensional position.

Simulations were performed of measurements on fresh fuel assemblies that included both calibration assemblies as well as “unknowns” that were unpoisoned, contained burnable poisons, or contained replacements with depleted uranium rods in accordance with the Office of International Nuclear Safeguards’, Safeguards Technology “Neutron Detector Rodeo” Task Plan. Typically, simulation runs in fast mode consisted of between 3.54×10^7 and 3.71×10^7 source neutrons, corresponding to measurement times between 708 and 732 s. The Obninsk energy spectrum was used for the ^{241}Am/Li source neutrons.

2.2 ANALYSIS

Analysis of the PSD plastic collar simulated data had a number of desirable goals in addition to evaluating the detector for the purposes of quantifying fresh fuel. These included:

- Identifying how to separate neutron-neutron coincidences originating from fission from those originating from inter-detector scatter,
- Identifying whether neutron-neutron coincidences from fission are detected in proportion to the number of induced fissions,
- Assessing the uniformity of response of the detector across the fuel assembly and identifying whether significant systematic errors are introduced by the particular detector geometry, and

- Assessing whether detector segmentation introduces significant advantage compared to detectors without segmentation for separating fission coincidences from inter-detector scatter.

Furthermore, the process by which the proposed system is calibrated and evaluated for health should be easily performed in the field, and the method by which true fission coincidences are extracted from a complicated data set should be straightforward and transparent to the inspector.

2.2.1 Fission Coincidences vs. Scatter Coincidences

The differences between neutron-neutron coincidences originating from fission and inter-detector scatter were investigated in a long simulation consisting of 3.236×10^{8} source neutrons incident on a 17×17 element fresh fuel assembly having a linear density of 65 g/cm ^{235}U. This configuration corresponds to the highest enrichment of the calibration configurations, as will be seen in Sect. 3.1. The distribution of induced fission within the assembly was saved in a histogram, having one bin for each fuel pin in the assembly, with the appropriate bin incremented for each instance of fission. The distribution of fission within the 65-g/cm ^{235}U fuel assembly is shown pictorially in Fig. 2; on the left, it is superimposed on the schematic diagram of the detector.

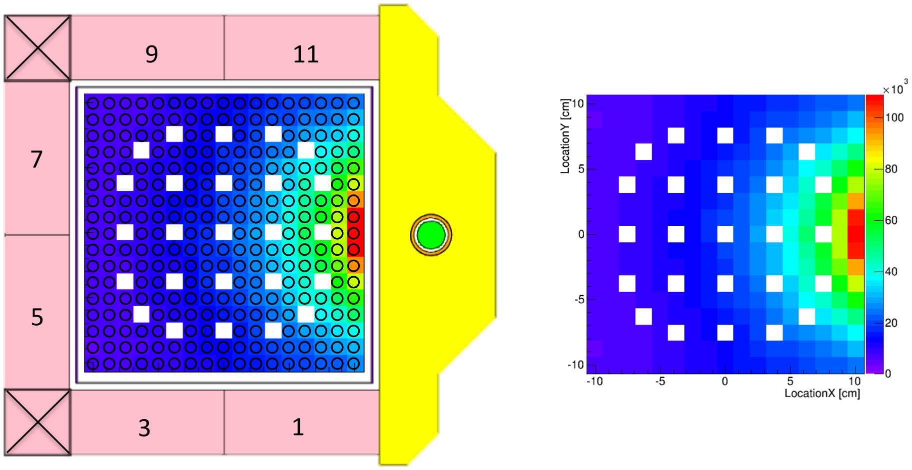

Fig. 2. The distribution of induced fission within a fuel assembly having 65 g/cm ^{235}U linear density (right) superimposed on the detector schematic diagram (left).

As might be expected, most of the fission takes place directly in front of the source. As an example, the fuel pin directly in front of the source has 20.5 times more induced fission than the pins in the farthest corners from the source. These fissions emit neutrons that can then be detected in the PSD plastic detectors. For each neutron detection, its attributed position (that corresponds to the energy-weighted average position of deposited energy) incremented the bin in a histogram that corresponded to its pixel position on the detector surface that faces the fuel. The resultant neutron hit pattern of attributed locations is shown in (a) of Fig. 3. Here, the detector panel is viewed as if it were unfolded and viewed from the source side, and each histogram bin corresponds to a detector pixel. Neutrons are detected in greater frequency in detectors 1, 2, 11, and 12 because they are adjacent to the source. Note that there are more neutron detections below the centerline because the neutron source is located slightly below the centerline of the detectors.

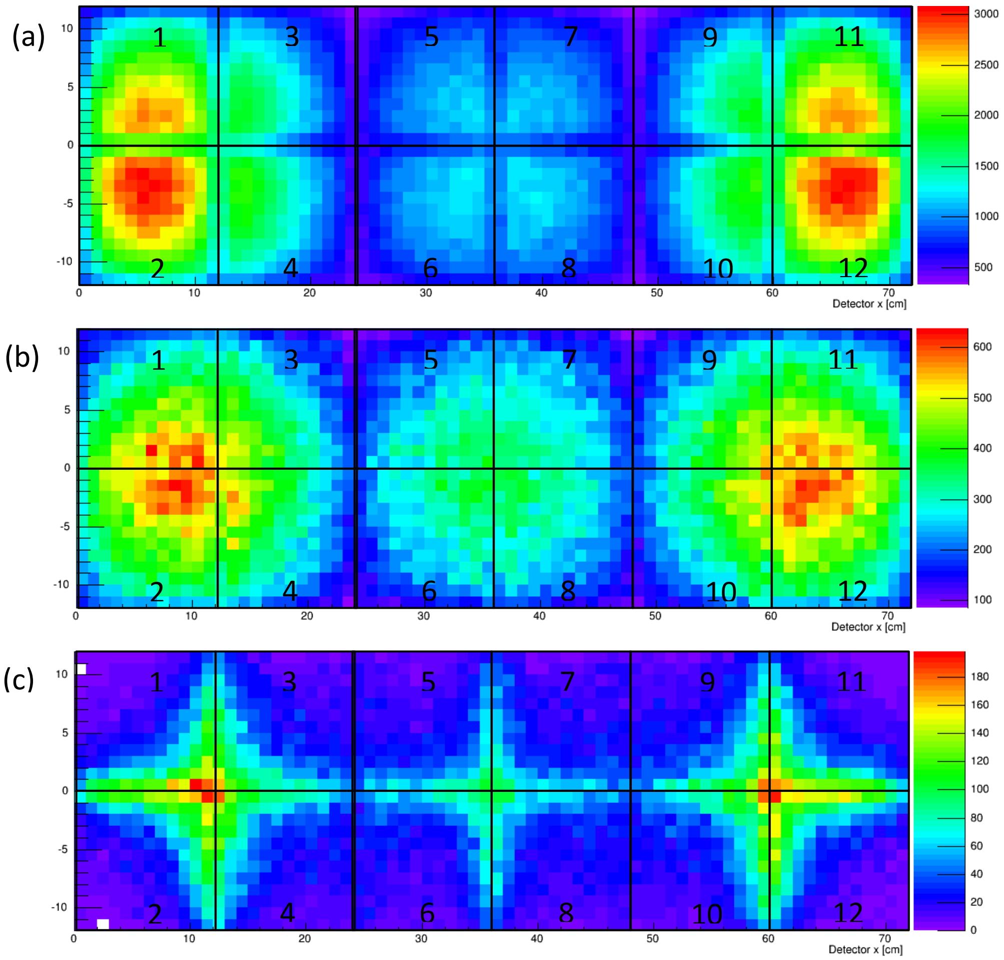

Fig. 3. Hit patterns on the detector panel from the vantage point of the source: (a) shows the hit pattern of neutrons on the detectors, (b) shows the hit pattern of neutron-neutron coincidences, and (c) shows the subset of those coincidences that consist of inter-detector scatter.

Likewise, for each coincident pair of neutrons, the attributed position of each neutron was used to increment a histogram of the detector surface that faces the fuel in 1-cm bins. The resultant neutron-neutron coincidence hit pattern is shown in panel (b) of Fig. 3. This hit pattern consists of all neutron-neutron hits, including coincidences originating from inter-detector scattering. Note that the coincidences are more evenly distributed across the detectors than the neutrons because there is more detector efficiency farther from the neutron source. Using the interaction histories in the PTRAC file, neutron-neutron coincidences originating from inter-detector scattering were identified and their attributed positions used to increment another histogram. The resultant inter-detector scattering hit pattern is shown in panel (c) of Fig. 3. Not surprisingly, the majority of detected scattering events occur along the boundaries between detectors because scattering that takes place within a detector is not inter-detector scattering. Also note that the boundaries in the corners have shielding between them (e.g., between detectors 3 and 5), and consequently have fewer instances of inter-detector scattering.

These very different distributions suggest that it is possible to distinguish inter-detector scattering from true neutron-neutron coincidences. For neutron-neutron coincidences, each neutron has an attributed position and time. Consequently, the two detections are separated by a distance $\boldsymbol{d}$ and time $\boldsymbol{\Delta t}$, as shown schematically in Fig. 4.

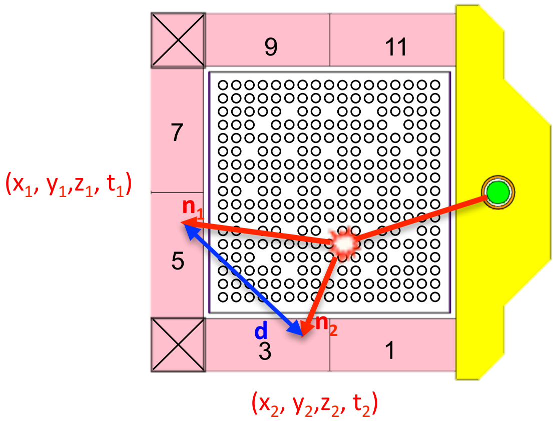

Fig. 4. Schematic diagram of the detection of two neutrons. The two detections are separated by distance d and time Δt.

In instances of inter-detector scattering, the neutron has to travel from the first interaction point to the second with the scattered velocity v_s. In contrast, true neutron-neutron coincidences are likely to occur either at exactly the same time or nearly the same time no matter where the two hits occur. Consequently, the relative distances and times were used to increment two-dimensional histograms of distance and time, shown in Fig. 5 for (left) scatter coincidences and (right) fission coincidences.

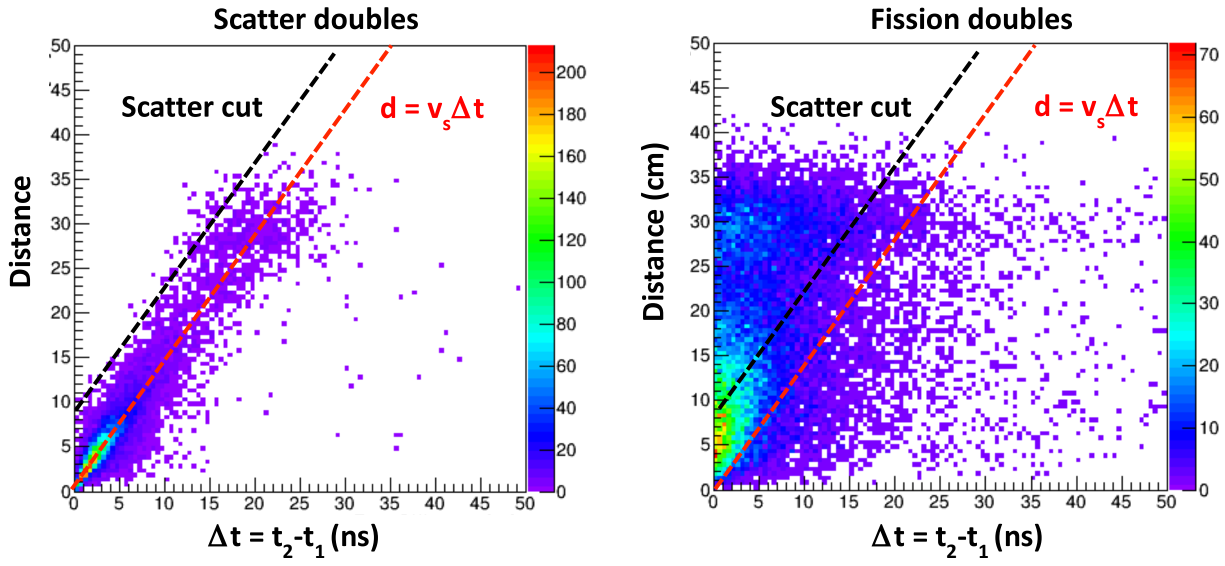

Fig. 5. Relative distance vs. time difference histograms for (left) inter-detector scattering and (right) fission neutrons.

Interestingly, the counts originating in inter-detector scattering fall along a trajectory $d = v_s t$, shown on the distance-time histograms by the dashed red line, and corresponding to an effective scattering velocity v_s. Note that further analysis of the simulations indicated that the effective scattering velocity primarily depends on the neutron detection threshold. Also note that a cut in this distance-time space can eliminate nearly all inter-detector scattering and identify a sample of nearly pure fission events. An example distance-time cut is shown on each histogram by the dashed black line. Now, we can consider the origin of induced fissions that give rise to the counts we observe, both in total and in the fission cut.

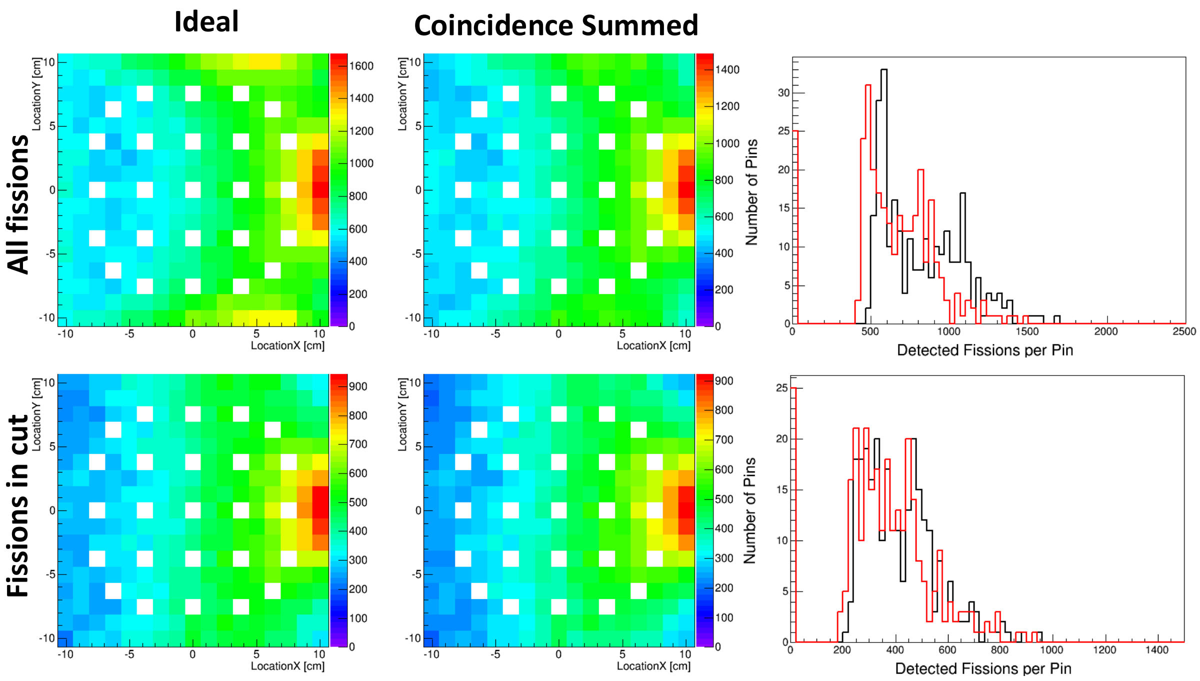

Fig. 6. The number distribution of fissions per fuel pin, shown as images (left) and as histograms (right). Images are shown for ideal counting and coincidence-summed counting for all doubles from fission as well as just those whose coincidences fall within the fission cut. The corresponding histograms for (black) idealized response and (red) coincidence-summed response show an overall drop in efficiency but approximately the same spread.

The detected fissions per fuel pin are shown in Fig. 6 for (upper left) idealized detection for all fission doubles, (lower left) idealized detection of fissions whose coincidences fall within the fission cut, (upper center) coincidence-summed detection of all fission doubles, and (lower center) coincidence summed detection of fissions whose coincidences fall within the fission cut. Histograms of the (black) idealized detection and (red) coincidence-summed detection are shown for (upper right) all fission doubles and (lower right) fission doubles that fall within the fission cut. Note that while coincidence summing changes the overall efficiency for detection of fissions, it does not appreciably change the spread in sensitivities to fuel pins. In this data, when considering all fission doubles and idealized counting, there was an average of 825 detected fissions per pin with a standard deviation of 259 for a relative spread of 0.31. Similarly, when considering all fission doubles but coincidence-summed counting, there was an average of 695 detected fissions per pin with a standard deviation of 210 for a relative spread of 0.30, that is, nearly identical pin-to-pin variability. When considering fission doubles in the fission cut, the average and standard deviations are 422 and 142 for idealized counting, giving a relative spread of 0.34, and 400 and 143 for coincidence-summed counting, giving a relative spread of 0.36. Consequently, it can be seen that coincidence summing is not a major contributor to the spread in sensitivity per fuel pin. Instead, the distance from the source is the largest factor contributing to the spread in per-pin sensitivities. Although not simulated in the present work, the drop in efficiency with distance from the source can be counteracted by increasing the number of detectors on the side opposite the source.

Because the inter-detector scattering falls along a linear trajectory, the two-dimensional space shown above is needlessly complicated. Instead, a one-dimensional histogram can be formed of the "excess time" $t_E = \frac{d}{v_s} - \Delta t$. This time corresponds to the difference between the expected time difference for scattering, d/v_s, and the measured one Δt. Histograms of excess time for (black) inter-detector scattering and (blue) fission are shown in Fig. 7. Note that the blue fission curve in Fig. 7 uses the ideal response where each neutron is counted separately, even if multiple neutrons hit the same detector.

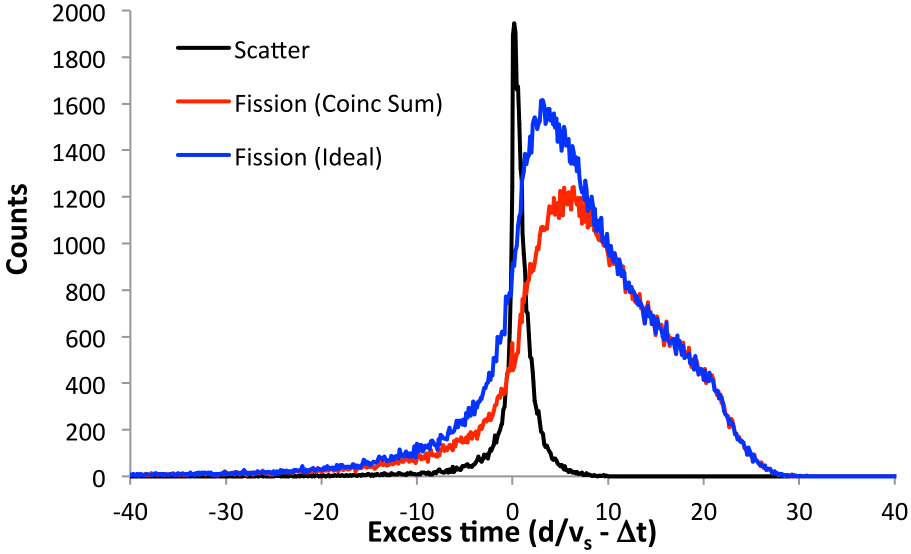

Fig. 7. Histograms of "excess time" for (black) inter-detector scatter and (blue) fission.

The same histogram was also made for the more realistic response where coincidence summing was taken into account. In this case, there is a loss of efficiency corresponding to multiple particles summing and being identified as a single particle. The coincidence-summed response is shown in red on Fig. 7. We will see later that because much of that loss of efficiency is in the region of excess time where the fission and scatter counts overlap, it will not be too detrimental to performance.

A particular measurement will have contributions to the excess time histogram from both scatter and fission. If we know the shape of the scatter and fission contributions (such as in Fig. 7 above), then it is possible to separately solve for the fission and scatter contributions. By integrating the counts in a scatter window S centered on the scatter peak and a fission window F that corresponds to times not in the scatter peak, it is then possible to solve for the doubles due to scatter D_S and the doubles due to fission D_F. (Note that the shape of the scatter contribution can be directly and quickly measured by counting an ^{241}Am/Be neutron source or more slowly by counting the ^{241}Am/Li interrogating neutron source.)

In an assay measurement, the counts S in the scatter gate will equal

$$S = D_F p_{fs} + D_S p_{ss},$$

and the counts in the fission gate will equal

$$F = D_F p_{ff} + D_S p_{sf},$$

where p_{fs} is the probability that a fission will be in the scatter gate, p_{ss} is the probability that a scatter will be in the scatter gate, p_{ff} is the probability that a fission will be in the fission gate and p_{sf} is the probability that a scatter will be in the fission gate. Since each neutron pair has to be in one or the other gate, then $p_{ff} + p_{fs} = 1$ and $p_{sf} + p_{ss} = 1$. We can solve for the doubles due to fission, D_F, to get

$$D_F = \left(\frac{1}{p_{ff} - p_{fs}\dfrac{p_{sf}}{p_{ss}}}\right)F - \left(\frac{1}{p_{ff}\dfrac{p_{ss}}{p_{sf}} - p_{fs}}\right)S.$$

Likewise, the doubles due to scattering, D_S, is

$$D_S = \left(\frac{1}{p_{sf} - p_{ss} \frac{p_{ff}}{p_{fs}}} \right) F - \left(\frac{1}{p_{sf} \frac{p_{fs}}{p_{ff}} - p_{ss}} \right) S.$$

Assuming the probabilities p_{ff}, p_{fs}, p_{ss}, and p_{sf} to be well known, then the statistical error in D_F is

$$\sigma_{D_F} = \sqrt{\left(\frac{1}{p_{ff} - p_{fs} \frac{p_{sf}}{p_{ss}}} \right)^2 F + \left(\frac{1}{p_{ff} \frac{p_{ss}}{p_{sf}} - p_{fs}} \right)^2 S}.$$

We can choose a scatter window width to minimize the statistical error in determining the number of true fission doubles D_F. For this purpose, it is straightforward to try all widths up to 20 ns, calculate F, S, and the probabilities p_{ff}, p_{fs}, p_{ss}, and p_{sf}, and then infer the error σ_{D_F}. This has been done and is shown in Fig. 8, where the red curve shows the statistical error of a 600-s measurement of idealized counting where no neutrons are missed due to coincidence summing. In this case, the best scatter-window width is approximately 3 ns, and the corresponding error is about 0.86%. In comparison, the black curve shows the corresponding calculation of the realistic situation where neutrons are lost due to coincidence summing. In this case, the best scatter-window width is still about 3 ns, but the corresponding error has increased modestly to 0.91%. That is, despite a reduction in efficiency of ~25% for fission doubles due to coincidence summing, the error only increases by ~5%. For the 3-ns scatter window, coincidence-summed data, the equation for the fission doubles D_F becomes:

$$D_S = 1.147F - 0.428S,$$

and the error in doubles becomes:

$$\sigma_{D_F} = \sqrt{1.316F + 0.183S}.$$

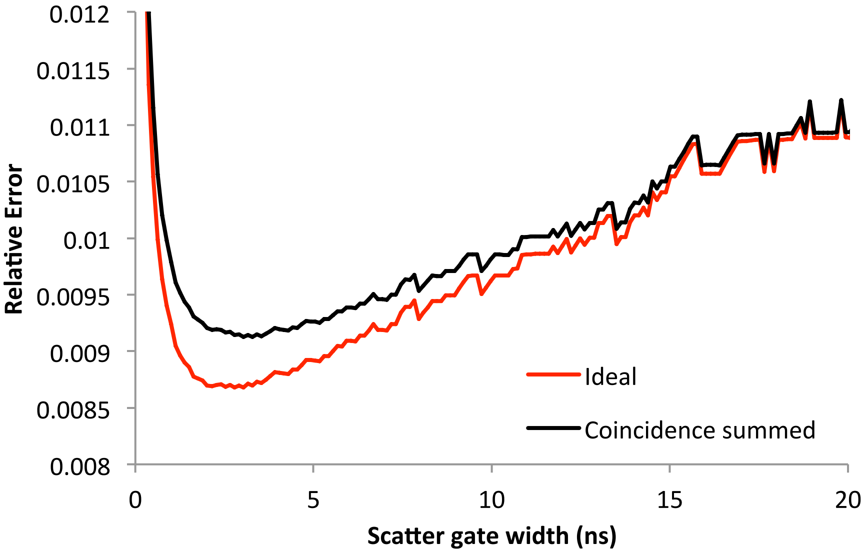

Fig. 8. Statistical error for a 600-s measurement for (red) realistic counting, that is, coincidence summed, in comparison to (black) idealized counting where no neutrons are missed. Note the suppressed zero on the y axis emphasizes the difference.

Last of all, it is important to show that the fission doubles D_F that we have extracted in this way are proportional to the number of fissions. For the calibration data that will be shown in Sect. 3.1, the extracted fission doubles are plotted as a function of the number of induced fissions and shown in Fig. 9. The slope of the line fitting the data indicates that there are 0.0286 detected doubles per induced fission. Further simulations would be desirable to show that a significant additional singles rate (such as might be encountered from nearby fuel in a nuclear facility) does not contribute significantly to systematic error.

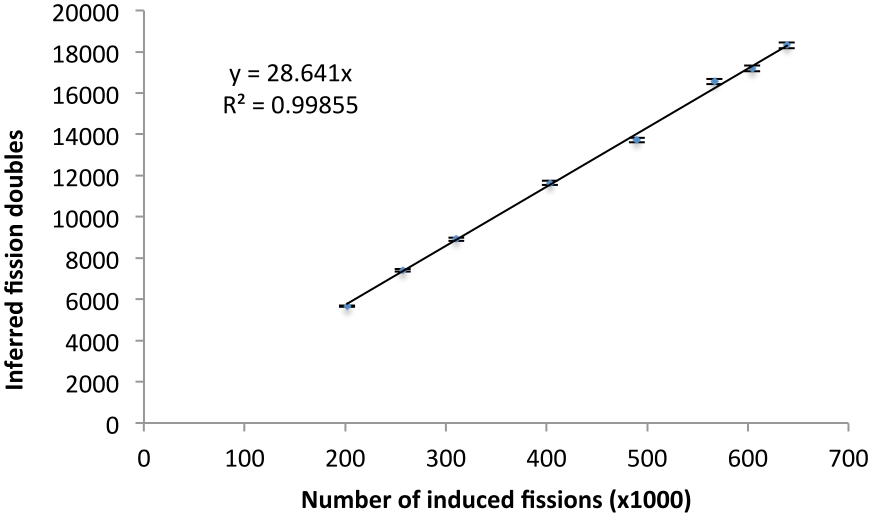

Fig. 9. Extracted fission doubles D_F as a function of the number of fissions. Note that D_F provides a good estimate of the number of fissions.

2.2.2 The Benefit of Segmentation

In part, use of segmented detectors was intended to enable better identification of the inter-detector scattering component of neutron-neutron coincidences. As was shown in Fig. 7, the fine segmentation of the detectors contributes to the ability to confine the inter-detector scattering component of coincidences to a narrow range of excess times. The narrower the scatter distribution, the less scatter double counts detract from the statistical accuracy of the determination of true fission doubles. Although detector segmentation gives a performance gain in terms of position resolution, it also exacts a toll in terms of light collection, as well as system complication. As a result, it was desirable to quantitatively assess the benefit of segmentation for eliminating inter-detector scattering.

For this investigation, the detectors still consist of 12 PSD plastic volumes, each 12 × 12 cm on a face with a depth of 5 cm arranged in a 2 × 2 array on each of three sides. However, the 12 × 12-cm face of the detector could be segmented into pixels as small as 1 × 1 cm (the same pixel pitch as present detectors) or as large as 6 × 6 cm (essentially one pixel per PMT). For the larger pixel pitches, corresponding to many fewer pixels, the inter-pixel distances were not binned in common distance bins. Instead, the detectors were considered pairwise and the average inter-detector scatter time subtracted. In this way, a similar excess time histogram was formed; however, in this case, it has the opposite sign as in Fig. 7. The (red) inter-detector scatter excess time distributions and (blue) fission distributions are shown for (left) 1-cm pixels and (right) 6-cm pixels in Fig. 10. Note that these time excess distributions are for idealized response where coincidence summing was not considered.

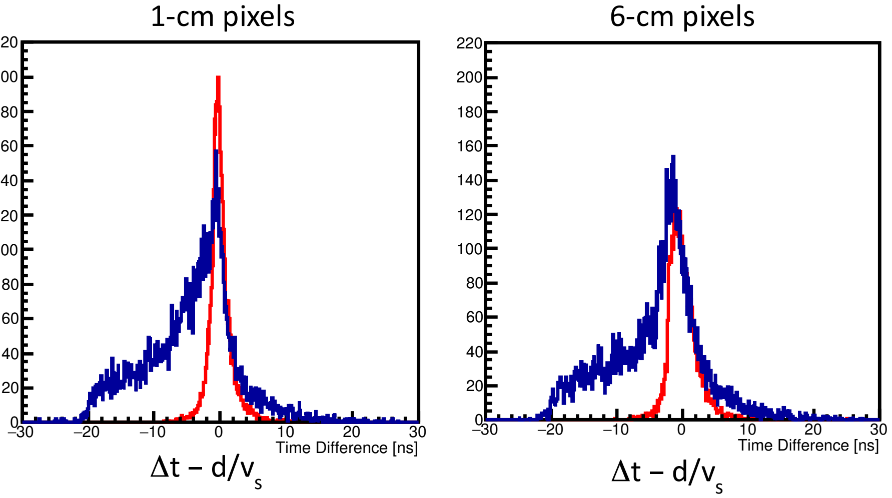

Fig. 10. Excess time histograms of (red) inter-detector scattering and (blue) fission for (left) 1-cm pixels and (right) 6-cm pixels.

For larger pixels, the inter-detector scatter counts form a wider peak as expected. This wider scatter peak with more overlap with the fission distribution affects the analysis two ways: First, it increases the statistical error in solving for the true fission counts, and second, it makes the task of inferring the shape of the fission coincidence distribution from the measured total and scatter distributions more difficult. In the present work, we will not address the second issue, but we will address the statistical error of subtraction given the above fission and scatter time excess distributions. For this purpose, the scatter window width was varied and the error in the number of true fission doubles calculated. Like before, all scatter-window widths up to 20 ns were tried, and F, S, and the probabilities p_{ff}, p_{fs}, p_{ss}, and p_{sf} were calculated to infer the error σ_{D_F}. This error is shown as a function of scatter gate width for (red) 6-cm pixels and (blue) 1-cm pixels in Fig. 11.

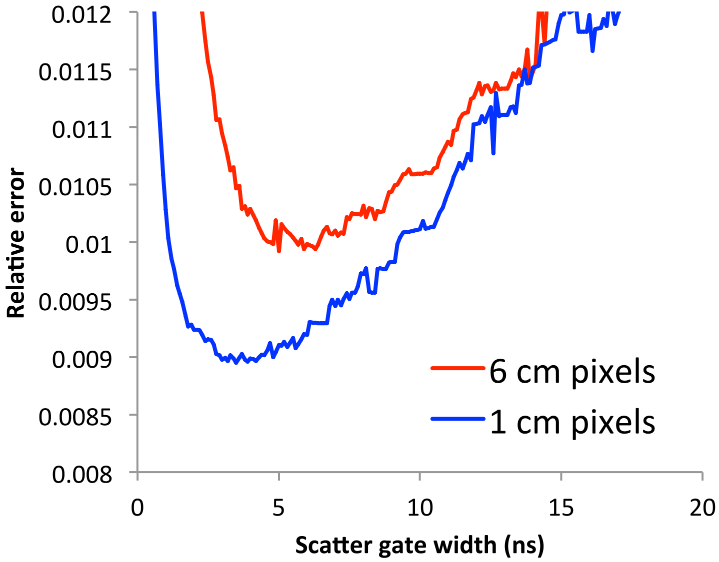

Fig. 11. Statistical error for a 600-s measurement for (red) 6-cm pixels and (blue) 1-cm pixels. Note the suppressed zero on the y-axis emphasizes the difference.

The error minimizing scatter-window width for 1-cm pixels is approximately 3 ns, and the corresponding error is about 0.9%. (This error is slightly different from that reported in Fig. 8, but it is derived from a different data set.) In comparison, the error minimizing scatter-window width for 6-cm pixels is about twice that, or 6 ns, consistent with the wider width of the scatter distribution. In this case, the corresponding error has increased by about 10% from approximately 0.9% to approximately 1%. Although the detector segmentation does provide identifiable benefit, similar benefit could be achieved via other means, such as increasing the detector efficiency. The majority of the benefit of using segmented detectors is not likely to be an increase in the statistical precision, but rather in having sufficient resolution to be able to decompose the excess time spectrum into the scatter and fission components that is necessary for this method to work.

3. RESULTS OF SIMULATIONS OF FRESH FUEL

3.1 CALIBRATION

Calibration of the PSD Plastic Collar was performed in both thermal and fast mode using a set of pressurized water reactor 17×17 virtual feed assemblies having 264 fuel pins and 25 guide tubes with a range of ^{235}U linear densities between 15 g/cm and 65 g/cm as specified by the task plan and listed in Table 1. The fuel was further specified with an assembly width of 21.4 cm, pin pitch of 1.278 cm, pellet density of 10.41 g/cm^3, pellet diameter of 0.8255 cm, and surrounded by cladding having an inner diameter of 0.836 cm, outer diameter of 0.95 cm, and density of 6.55 g/cm^3.

Table 1. Details on the calibration assemblies, as specified in the task plan

^{235}U (g/cm)	Enrichment (%)	^{235}U wt%	^{238}U wt%
15	1.16	0.01023	0.87127
20	1.54	0.01358	0.86792
25	1.93	0.01701	0.86449
35	2.70	0.02380	0.85770
45	3.47	0.03059	0.85091
55	4.24	0.03738	0.84412
60	4.63	0.04081	0.84068
65	5.01	0.04416	0.83734

The coincidence-summed response was simulated, and for neutron-neutron pairs, the relative time and distance were used to calculate an excess time. The fission (F) and scatter (S) window counts on the excess time histogram were summed and used to calculate the fission doubles rate D_F. Simulations were performed for fast mode and for thermal mode.

3.1.1 Fast Mode Calibration

A summary of the simulated rates for the fast-mode calibration data is shown in Table 2. In this simulation, a 1-mm-thick Cd liner was incorporated that extended 17 cm in either direction from the centerline of the ^{241}Am/Li source.

Table 2. Results of simulations for the "fast mode" calibration, where *F* and *S* are the fission and scatter window count rates, respectively, and D_F is the inferred fission doubles rate

L_{235} (g/cm)	Source particles	$t_{equiv.}$ (s)	Neuts (s^{-1})	F (s^{-1})	S (s^{-1})	D_F (s^{-1})	ΔD_F (s^{-1})
15	3.66E+07	731.9	196.0	7.59	2.26	7.74	0.12
20	3.64E+07	728.8	215.1	9.86	2.68	10.17	0.14
25	3.63E+07	726.1	234.0	11.90	3.20	12.28	0.15
35	3.60E+07	720.9	268.2	15.52	3.84	16.15	0.17
45	3.58E+07	716.3	298.8	18.41	4.56	19.15	0.19
55	3.56E+07	712.2	328.7	22.24	5.28	23.24	0.21
60	3.55E+07	710.1	342.2	23.18	5.55	24.21	0.21
65	3.54E+07	708.2	354.4	24.72	5.79	25.87	0.22

The data were fitted to the functional form

$$D_F = \frac{aL_{235}}{1 + bL_{235}},$$

where L_{235} is the linear density of ^{235}U in g/cm, a is a proportionality constant that equals the number of detected neutron coincidences per linear density of ^{235}U, and b is another constant that characterizes the rate at which the interrogation neutrons are used up by the presence of ^{235}U in the fuel assembly. The doubles rate was plotted as a function of linear density and shown by the blue points in Fig. 12, along with its fit, shown by the blue curve, and comparison to the canonical calibration for the UNCL, shown by the red curve. By eye, the calibration curve for the PSD plastic collar is essentially identically 1.3 times that of the UNCL.

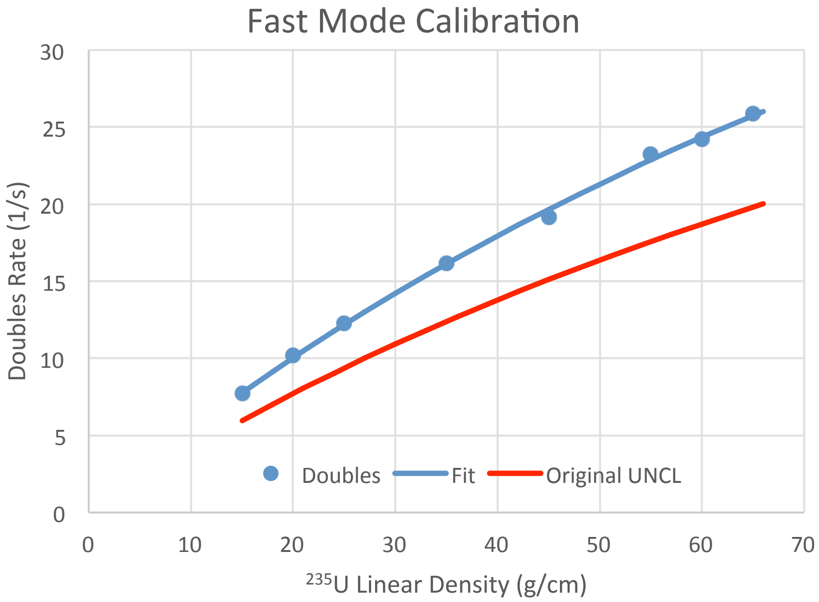

Fig. 12. Fast mode calibration (points) simulated data, (blue) fit to data, and (red) canonical calibration curve for the UNCL.

The fitted values are $a = 0.5705 \pm 0.0074$ and $b = 0.006775 \pm 0.00036$. The covariance values for the fit are $(a{:}\,a)$ $5.4702{\times}10^{-5}$, $(a{:}\,b)$ $2.5594{\times}10^{-6}$, and $(b{:}\,b)$ $1.2992{\times}10^{-7}$.

3.1.2 Thermal Mode Calibration

A summary of the simulated rates for the thermal-mode calibration data is shown in Table 3. In this simulation, there was no Cd liner.

Table 3. Results of simulations for the "thermal mode" calibration, where F and S are the fission and scatter window count rates, respectively, and D_F is the inferred fission doubles rate

L_{235} (g/cm)	Source particles	$t_{equiv.}$ (s)	Neuts (s^{-1})	F (s^{-1})	S (s^{-1})	D_F (s^{-1})	ΔD_F (s^{-1})
15	2.57E+07	513.6	1297.5	125.75	27.71	132.33	0.58
20	2.51E+07	501.8	1478.8	144.97	31.72	152.66	0.63
25	2.46E+07	492.5	1623.4	159.25	35.22	167.53	0.66
35	2.40E+07	479.8	1836.9	181.82	40.01	191.36	0.72
45	2.35E+07	471.0	1985.0	196.70	43.57	206.90	0.75
55	2.32E+07	464.3	2105.2	208.93	46.13	219.83	0.78
60	2.31E+07	461.5	2156.4	214.59	47.45	225.76	0.79
65	2.29E+07	458.8	2209.0	220.81	48.64	232.37	0.81

The simulated data were fitted to the same functional form as for the fast-mode data. The (blue points) doubles rate was plotted along with the (blue curve) fit as a function of linear density, and it is shown in Fig. 13. Comparison to the canonical calibration for the UNCL is shown by the red curve. Note that the shape is significantly different in thermal mode, with the PSD plastic collar detecting about 25% more coincidences at low enrichment, but about the same number of coincidences at high enrichments. The origin of this difference is not presently known, but it is hypothesized that the PSD plastic detectors saturate earlier because the absence of ^{3}He tubes allows them to moderate neutrons more effectively than the ^{3}He panels of the UNCL, but the smaller vertical extent of the PSD plastic collar makes the overall efficiency for thermalizing neutrons smaller.

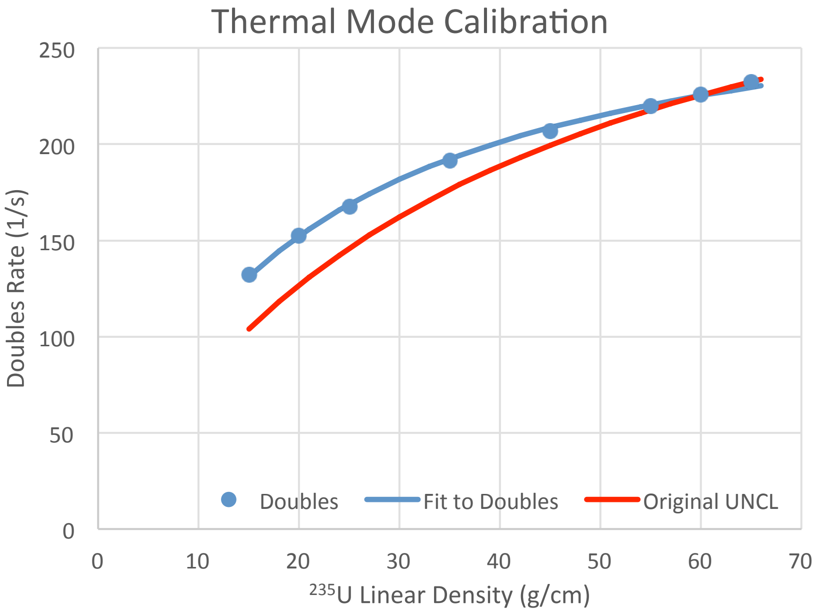

Fig. 13. Thermal mode calibration (points) simulated data, (blue) fit to data, and (red) canonical calibration curve for the UNCL.

The fitted values are $a = 15.673 \pm 0.128$ and $b = 0.05289 \pm 0.00064$. The covariance values for the fit are $(a\colon a)$ 0.01629, $(a\colon b)$ 8.089×10^{-5}, and $(b\colon b)$ 4.126×10^{-7}.

3.2 EVALUATION OF UNPOISONED UNKNOWNS

Evaluation of the PSD plastic collar was performed using unpoisoned assemblies having a range of fuel assembly sizes and enrichments. A total of 12 unpoisoned configurations spanning commonly used fuel assemblies in industry having sizes of 14×14, 15×15, 16×16, and 17×17 fuel rods were simulated. Specifications for common fuel assemblies are tabulated in Table 4. Configurations that were simulated have a letter (A, B, C, or D) in the “label” column. The results were analyzed using the appropriate thermal or fast mode calibration curve for 17×17 fuel assemblies. In general, the statistical errors in the doubles rates were better than 1% for 600-s measurements of all configurations, but analyzed mass defects were in some cases greater than 10%. The origin of the analyzed mass defects appears to be differences in the average efficiency with which fission neutrons can escape from the fuel assemblies to be detected by the collar. These different efficiencies are, in turn, caused by differences in the average density of assemblies due to differing pellet densities or fuel spacing for different fuel designs. As such, the analyzed mass defects are likely to be similar for all collar designs involving fast neutron detectors.

Table 4. Fuel specifications for fuel assemblies commonly used in industry, as specified in the task plan

Label	Assembly Size AAxAA	Assembly width (cm)	Pin Pitch (cm)	# Fuel Pins	# Guide Tubes	Cladding	Clad OD (cm)	Clad thickness (cm)	Pellet density (g/cm^3)	Pellet OD (cm)	Manufacturer and design
A,C	14	19.70	1.437	179	17	Zirlo	1.016	0.0617	10.42	0.875	KNFC OFA
	14	19.72	1.434	179	17	Zr4	1.072	0.0620	10.40	0.929	AFA 3G
B	14	20.60	1.499	176	20	Zr4	1.118	0.0660	10.44	0.968	Westinghouse CE
	14	19.70	1.433	179	17	Imp.Zr4	1.072	0.0620	10.64	0.929	Mitsubishi
C	15	21.70	1.472	208	17	Zr4	1.090	0.0635	10.52	0.940	Mk-B
B	15	21.50	1.459	205	20	Zirlo	1.075	0.0725	10.45	0.911	FOCUS-X5
A	15	21.40	1.452	204	21	Imp. Zr4	1.072	0.0620	10.64	0.929	Mitsubishi
	16	20.70	1.315	236	20	Zr4	0.970	0.0635	10.30	0.826	Westinghouse CE
A	16	19.70	1.252	235	21	Zirlo	0.914	0.0572	10.42	0.784	KNFC ACE7
D	16	22.96	1.459	236	20	Zr4	1.075	0.0725	10.50	0.911	WH Sweden & EFG
B,C	16	20.70	1.317	236	20	Zirlo	0.950	0.0572	10.42	0.819	KNFC Plus7
	16	20.70	1.315	236	20	Zirlo	0.970	0.0640	10.45	0.826	KNFC KSD
	17	21.40	1.278	264	25	Zirlo	0.950	0.0572	10.42	0.819	KNFC ACE7 or FORTE
A	17	21.40	1.278	264	25	Zr4	0.950	0.0570	10.52	0.819	Mk-BW17
B	17	21.40	1.278	264	25	Imp. Zr4	0.950	0.0570	10.64	0.819	Mitsubishi

3.2.1 Fast Mode Simulations of Unpoisoned Unknowns

A summary of the simulated rates for the range of different fuel configurations measured in fast mode is shown in Table 5. Note that in fast mode the statistical error of the measurement of fission doubles is approximately 1% for all simulated measurements.

Table 5. Results of simulations for a range of fuel assemblies in fast mode, where F and S are the fission and scatter window count rates, respectively, and D_F is the inferred fission doubles rate

Name	Source particles	$t_{equiv.}$ (s)	Neuts (s^{-1})	F (s^{-1})	S (s^{-1})	D_F (s^{-1})	ΔD_F (s^{-1})
14x14A	3.82E+07	764.5	299.6	17.54	4.15	18.34	0.18
14x14B	3.77E+07	753.4	284.8	16.62	3.98	17.35	0.17
14x14C	3.87E+07	773.3	237.1	10.69	2.84	11.04	0.14
15x15A	3.65E+07	729.9	338.9	23.39	5.55	24.45	0.21
15x15B	3.64E+07	729.0	350.2	24.20	5.86	25.24	0.21
15x15C	3.63E+07	726.4	341.7	23.26	5.58	24.28	0.21
16x16A	3.70E+07	739.2	324.9	20.83	4.75	21.85	0.20
16x16B	1.83E+07	366.0	328.3	21.52	5.20	22.45	0.28
16x16C	1.85E+07	370.3	266.9	14.68	3.67	15.26	0.23
16x16D	6.00E+01	709.9	339.9	24.14	5.94	25.14	0.22
17x17A	3.59E+07	718.1	289.8	17.93	4.48	18.64	0.18
17x17B	3.56E+07	712.7	326.5	21.59	5.08	22.58	0.20

Each of the above cases was used, along with the calibration curve (for 17×17 assemblies) of Sect. 3.1.1 to calculate the analyzed linear density. The error in the analyzed linear density takes into account the statistical uncertainty of a 600-s measurement along with the uncertainty of the calibration curve. The error does not take into account the fitness of that curve for the present fuel. The declared linear densities and analyzed linear densities (along with uncertainties) are tabulated in Table 6. The total uncertainty reported takes into account an assumed 2% systematic error.

Table 6. Declared and analyzed linear densities for the 12 unpoisoned fuel scenarios simulated in fast mode

Name	Declared L_{235} (g/cm)	Analyzed L_{235} (g/cm)	600 s L_{235} Uncert (g/cm)	600 s Total Uncert (%)	Mass Defect (%)
14x14A	37.57	41.09	0.60	2.48%	9.4%
14x14B	37.31	38.31	0.57	2.50%	2.7%
14x14C	19.78	22.27	0.40	2.69%	12.6%
15x15A	58.37	60.39	0.90	2.49%	3.5%
15x15B	61.54	63.19	0.95	2.50%	2.7%
15x15C	60.91	59.81	0.89	2.49%	-1.8%
16x16A	46.90	51.72	0.74	2.46%	10.3%
16x16B	50.16	53.66	0.78	2.47%	7.0%
16x16C	30.95	32.68	0.51	2.54%	5.6%
16x16D	64.07	62.81	0.95	2.50%	−2.0%
17x17A	41.29	41.97	0.62	2.48%	1.7%
17x17B	54.82	54.08	0.78	2.47%	−1.3%

A number of assemblies have significant mass defects (>5%). A positive mass defect means that there are more neutron-neutron coincidences detected per time than expected due to the calibration curve. The increase in doubles could originate from either a higher efficiency for inducing fissions or a higher efficiency for detecting neutron-neutron coincidences. For the present simulations, the number of fissions was recorded along with the extracted number of doubles from fission, and the combination was used to calculate the detected doubles per fission for each configuration. Then, the difference between the doubles per fission of that configuration and the calibration data was calculated and expressed as a percent. Fig. 14 shows the mass defect as a function of the excess doubles, and it suggests that the origin of the mass defects is an increase in efficiency for detecting neutron-neutron coincidences. Not shown in Fig. 14, configuration 16x16D does not fall on the trend, having an excess doubles per fission of 25% while the linear density defect is −2.0%. The reason for this anomaly is not presently known.

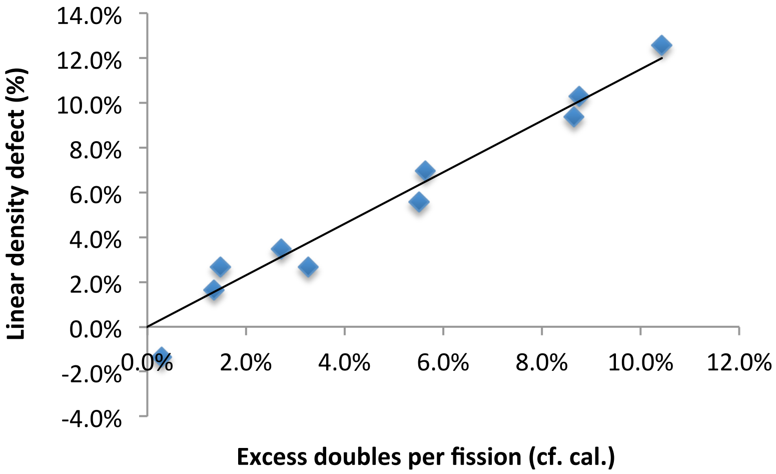

Fig. 14. The defect in linear density is plotted as a function of the difference between the simulated doubles per fission of each configuration compared to the calibration configuration (expressed in percent).

An inspection of the definitions of the fuel for the various configurations suggests that the primary reason for the additional efficiency for detecting neutron coincidences is an overall smaller average density for those fuel assemblies having a large defect. Simply stated, the fuels with higher defects have more open space in them through which neutrons can escape. A plot of the average density of the fuel assemblies under consideration is shown in Fig. 15.

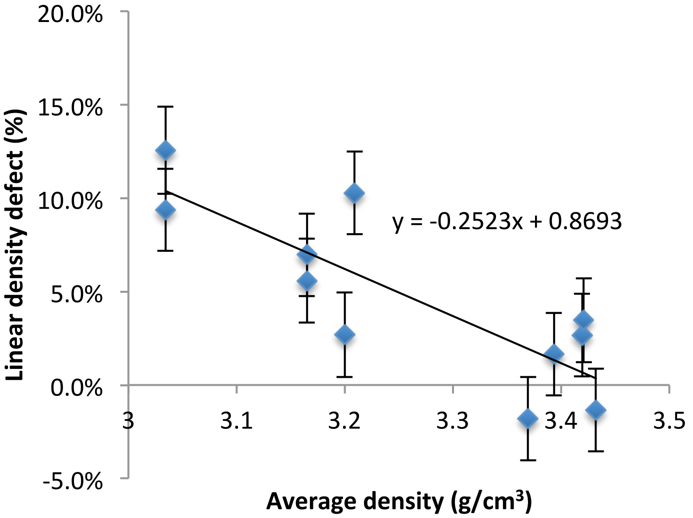

Fig. 15. The defect in linear density plotted as a function of the average density of the fuel assembly.

3.2.2 Thermal Mode Simulations of Unpoisoned Unknowns

No significant additional analysis was performed for the thermal mode simulations of the unpoisoned fuel configurations, but the results are reported for completeness. A summary of the simulated rates for the range of different fuel configurations measured in fast mode is shown in Table 7. Note that in thermal mode the statistical error of the measurement of fission doubles is approximately 0.35% for all simulated measurements.

Table 7. Results of simulations for a range of fuel assemblies in thermal mode, where F and S are the fission and scatter window count rates, respectively, and D_F is the inferred fission doubles rate.

Name	Source particles	$t_{equiv.}$ (s)	Neuts (s^{-1})	F (s^{-1})	S (s^{-1})	D_F (s^{-1})	ΔD_F (s^{-1})
14x14A	2.68E+07	536.0	1910.1	195.70	40.05	207.26	0.70
14x14B	2.60E+07	519.6	1872.9	186.23	40.07	196.39	0.70
14x14C	2.80E+07	559.6	1518.2	151.96	31.37	160.81	0.61
15x15A	2.42E+07	484.7	2147.0	214.16	47.12	225.39	0.77
15x15B	2.42E+07	483.6	2197.6	219.75	48.43	231.25	0.78
15x15C	2.40E+07	479.5	2166.8	215.31	48.04	226.33	0.78
16x16A	2.51E+07	501.5	2009.9	203.58	41.96	215.48	0.74
16x16B	2.45E+07	490.3	2078.3	211.59	44.85	223.43	0.76
16x16C	2.54E+07	507.4	1778.1	178.24	38.22	188.02	0.69
16x16D	2.28E+07	456.2	2229.8	220.09	51.77	230.21	0.81
17x17A	2.37E+07	473.6	1946.2	192.69	43.01	202.54	0.74
17x17B	2.32E+07	464.9	2105.7	210.21	46.39	221.18	0.78

Each of the above cases was used, along with the calibration curve (for 17×17 assemblies) of Sect. 3.1.2, to calculate the analyzed linear density. The error in the analyzed linear density takes into account the statistical uncertainty of a 600-s measurement along with the uncertainty of the calibration curve. The error does not take into account the fitness of that curve for the present fuel. The declared linear densities and analyzed linear densities (along with uncertainties) are tabulated in Table 8. The total uncertainty reported takes into account an assumed 2% systematic error. Note that the assemblies with large defects in linear density are the same assemblies that have large defects for the fast-mode measurements.

Table 8. Declared and analyzed linear densities for the 12 unpoisoned fuel scenarios simulated in thermal mode

Name	Declared L_{235} (g/cm)	Analyzed L_{235} (g/cm)	600 s L_{235} Uncert (g/cm)	600 s Total Uncert (%)	Mass Defect (%)
14x14A	37.57	43.99	0.51	2.31%	17.1%
14x14B	37.31	37.15	0.39	2.26%	−0.4%
14x14C	19.78	22.44	0.20	2.19%	13.4%
15x15A	58.37	60.07	0.90	2.49%	2.9%
15x15B	61.54	67.18	1.11	2.59%	9.2%
15x15C	60.91	61.13	0.93	2.51%	0.4%
16x16A	46.90	50.39	0.65	2.38%	7.4%
16x16B	50.16	57.94	0.84	2.47%	15.5%
16x16C	30.95	32.82	0.33	2.23%	6.0%
16x16D	64.07	65.82	1.07	2.58%	2.7%
17x17A	41.29	40.83	0.46	2.29%	−1.1%
17x17B	54.82	55.65	0.78	2.44%	1.5%

3.3 PARTIAL DEFECTS

Simulations were performed to assess the sensitivity of the PSD plastic collar for the detection of partial defects in the 17×17 fuel type. In these simulations, 8, 16, 24, 32, or 40 LEU rods having 4% enrichment were replaced with DU rods in the pattern specified by the task plan and shown in Fig. 16.

For fast mode, the statistical error of the doubles rate for 600-s counts was approximately 1% for these measurement simulations. The slope of the fast-mode calibration curve makes the ~1% error for doubles a ~1.5% error for analyzed linear density. Last of all, combination with an assumed 2% systematic error gives an overall uncertainty of about 2.5%. This total uncertainty means that the magnitude of the three standard deviation (3σ) defect would be 7.5% of an assembly, or about 20 pins of a 17×17 assembly. In the absence of any statistical error, an assumed 2% statistical error alone would give a 3σ defect of 6.0% of assembly, or 16 pins.

For thermal mode, the statistical error of the doubles rate for 600-s counts was approximately 0.35% for these measurement simulations. The slope of the fast-mode calibration curve makes the ~0.35% error for doubles a ~1.3% error for analyzed linear density. Last of all, combination with an assumed 2% systematic error gives an overall uncertainty of about 2.4%. Interestingly, because of saturation of the thermal mode calibration curve, the superior statistics of the thermal-mode measurements do not translate into better accuracy in analyzed linear density.

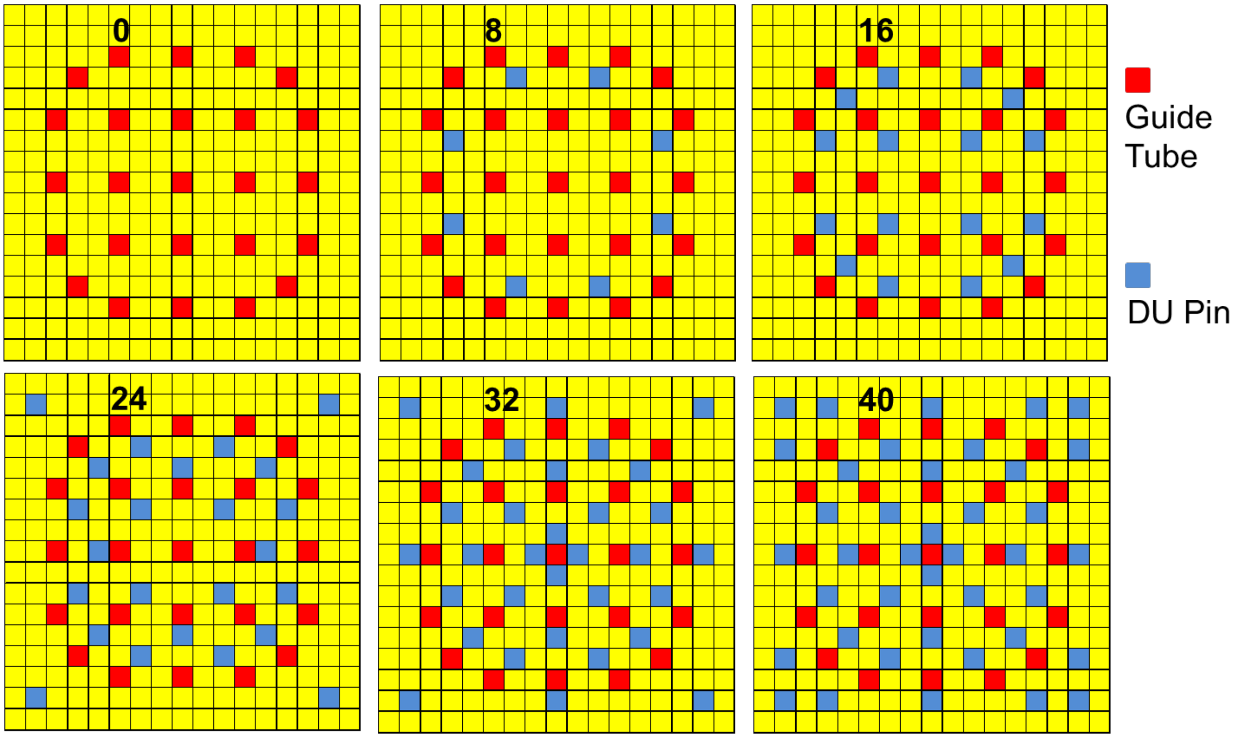

Fig. 16. The distribution of DU replacement pins in fuel assemblies as specified in the task plan to test sensitivity to detect partial defects.

3.3.1 Fast Mode Simulations of Partial Defects

A summary of the simulated rates for the partial defect configurations measured in fast mode is shown in Table 9. Note that in fast mode the statistical error of the measurement of fission doubles is approximately 1% for all simulated measurements.

Table 9. Results of simulations for partial defects in fast mode, where F and S are the fission and scatter window count rates, respectively, and D_F is the inferred fission doubles rate

Missing Pins	Source particles	$t_{equiv.}$ (s)	Neuts (s^{-1})	F (s^{-1})	S (s^{-1})	D_F (s^{-1})	ΔD_F (s^{-1})
0	3.57E+07	713.4	320.1	21.11	5.06	22.04	0.20
8	3.57E+07	714.0	315.9	20.43	4.96	21.30	0.20
16	3.57E+07	714.8	310.9	20.40	4.88	21.30	0.20
24	3.58E+07	715.3	308.5	19.78	4.70	20.66	0.19
32	3.58E+07	715.8	303.0	19.12	4.74	19.89	0.19
40	3.45E+07	690.5	298.6	18.63	4.59	19.40	0.19

Each of the above cases was used, along with the calibration curve of Sect. 3.1.1, to calculate the analyzed linear density. The error in the analyzed linear density takes into account the statistical uncertainty of a 600-s measurement along with the uncertainty of the calibration curve. The declared linear densities, actual linear densities, and analyzed linear densities (along with uncertainties) are tabulated in Table 10. The total uncertainty reported takes into account an assumed 2% systematic error.

Table 10. Declared, actual, and analyzed linear densities for the six fuel scenarios simulated in fast mode. Note that the mass defect is reported compared to the analyzed linear density with no pins missing

Missing Pins	Declared L_{235} (g/cm)	Actual L_{235} (g/cm)	Analyzed L_{235} (g/cm)	600 s L_{235} Uncert (g/cm)	600 s Total Uncert (%)	Mass Defect (%)
0	51.90	51.90	52.34	0.76	2.47%	0.0%
8	51.90	50.33	49.97	0.72	2.47%	−4.5%
16	51.90	48.77	49.98	0.72	2.47%	−4.5%
24	51.90	47.20	48.00	0.69	2.47%	−8.3%
32	51.90	45.63	45.66	0.66	2.47%	−12.8%
40	51.90	44.07	44.20	0.64	2.47%	−15.6%

The results of the partial defect simulations are also presented in graphical form in Fig. 17. Here, the mass defect of the analyzed linear density (relative to the analyzed linear density of the zero-defect case) is shown as a function of the number of missing pins. Note that the slope of the best-fit line should correspond to the fractional mass defect per missing pin. The numerical value of the best-fit line is -0.00380, within 1% of the value $-1/265$, the expected value of the mass defect per pin.

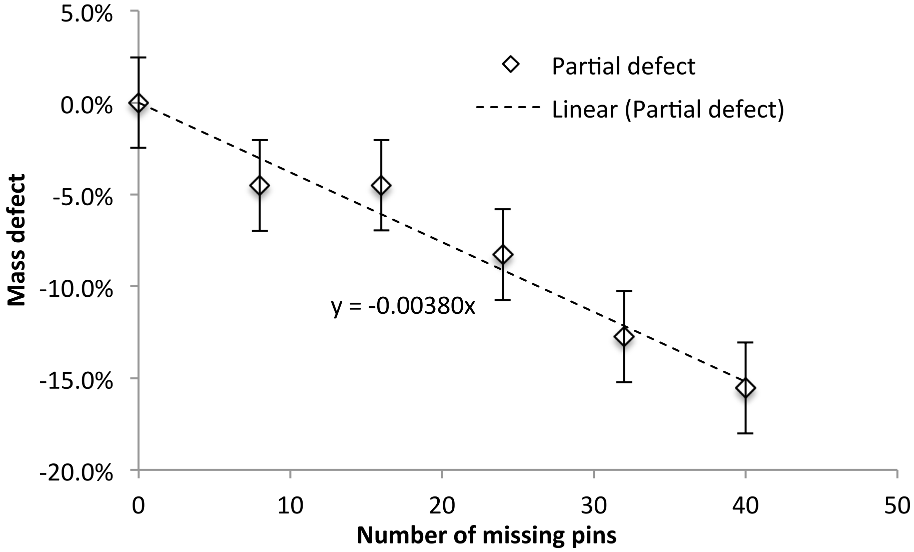

Fig. 17. The analyzed linear density defect as a function of the number of missing pins for the fast mode simulation of partial defects.

As a result, with a ~2.5% total uncertainty, a three standard deviation (3σ) defect would on average require removal of $0.075\times265 \approx 20$ pins. It is worth noting that even in the complete absence of statistical error, the assumption of 2% systematic uncertainty will mean that a 3σ defect would on average require removal of $0.06\times265 \approx 16$ pins. Consequently, the simulated performance of the PSD plastic collar in fast mode is close to the assumed systematic-limited performance.

3.3.2 Thermal Mode Simulations of Partial Defects

A summary of the simulated rates for the partial defect configurations measured in thermal mode is shown in Table 11. Note that in thermal mode, the statistical error of the measurement of fission doubles is approximately 0.35% for all simulated measurements.

Table 11. Results of simulations for partial defects in thermal mode, where F and S are the fission and scatter window count rates, respectively, and D_F is the inferred fission doubles rate.

Missing Pins	Source particles	$t_{equiv.}$ (s)	Neuts (s^{-1})	F (s^{-1})	S (s^{-1})	D_F (s^{-1})	ΔD_F (s^{-1})
0	2.33E+07	466.2	2071.5	205.70	45.15	216.54	0.77
8	2.34E+07	467.1	2063.9	204.44	45.83	214.81	0.77
16	2.34E+07	467.9	2050.8	203.40	44.21	214.30	0.77
24	2.27E+07	453.7	2029.8	202.34	44.90	212.80	0.78
32	2.35E+07	470.1	2011.9	199.15	44.61	209.27	0.76
40	2.36E+07	471.3	1989.9	196.73	43.54	206.94	0.75

Each of the above cases was used, along with the calibration curve of Sect. 3.1.2, to calculate the analyzed linear density. The error in the analyzed linear density takes into account the statistical uncertainty of a 600-s measurement along with the uncertainty of the calibration curve. Interestingly, although the statistical uncertainty of the number of doubles is much better in thermal mode, the slope of the calibration curve is sufficiently reduced that the mass uncertainties are nearly identical to those in fast mode. The declared linear densities, actual linear densities, and analyzed linear densities (along with uncertainties) are tabulated in Table 12. Again, the total uncertainty reported takes into account an assumed 2% systematic error.

Table 12. Declared, actual, and analyzed linear densities for the six fuel scenarios simulated in thermal mode

Missing Pins	Declared L_{235} (g/cm)	Actual L_{235} (g/cm)	Analyzed L_{235} (g/cm)	600 s L_{235} Uncert (g/cm)	600 s Total Uncert (%)	Mass Defect (%)
0	51.90	51.90	51.31	0.68	2.39%	0.0%
8	51.90	50.33	49.82	0.68	2.37%	−2.9%
16	51.90	48.77	49.39	0.68	2.37%	−3.7%
24	51.90	47.20	48.16	0.68	2.36%	−6.1%
32	51.90	45.63	45.44	0.67	2.33%	−11.4%
40	51.90	44.07	43.77	0.67	2.31%	−14.7%

The results of the partial defect simulations are also presented in graphical form in Fig. 18. Again, the mass defect of the analyzed linear density (relative to the analyzed linear density of the zero-defect case) is shown as a function of the number of missing pins. As before, the slope of the best-fit line should correspond to the fractional mass defect per missing pin. The numerical value of the best-fit line is -0.00336, slightly more than 1% different from the value $-1/265$, the expected value of the mass defect per pin.

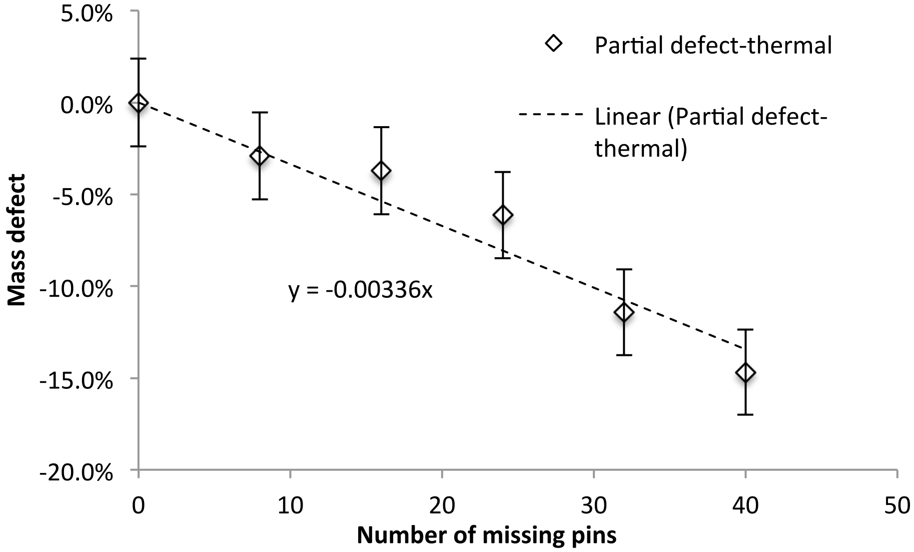

Fig. 18. The analyzed mass defect as a function of the number of missing pins for the thermal mode simulation of partial defects.

As a result, the ~2.4% total uncertainty yields a three standard deviation (3σ) defect that would on average require removal of $0.072\times265 \approx 19$ pins.

3.4 BURNABLE POISONS

The primary focus of the present study was to evaluate the assay of fuels containing burnable poisons in fast mode. For this purpose, the statistical accuracy and independence of these measurements from the burnable poison content was of particular interest. For fuels with burnable poisons, the removal of interrogating neutrons by neutron capture in the poison lowers the induced fission rate. Correction for the presence of burnable poison depends on operator-declared information regarding the linear density of burnable poison, and for higher burnable poison loadings, this correction can be as large as a factor of two in analyzed mass. Fast mode uses a Cd liner to eliminate the thermal neutron flux that is modified by the presence of burnable poison, and as a result, drastically reduces the sensitivity of the measurement to the amount of burnable poison. To evaluate the sensitivity of the PSD plastic collar to burnable poisons, fuel assemblies were simulated having 4, 8, 12, 16, 20, and 24 pins containing Gd in concentrations of 6%, 8%, and 10%. The pattern of Gd pins was as specified in the task plan and shown in Fig. 19.

As a result of these simulations, it is shown that in fast mode, the reduction of detected neutron-neutron coincidences is due to a reduction of fissions (by about 6% relative to that expected for the ^{235}U linear density for the largest Gd content). This reduction in induced fissions is simply a consequence of the energy spectrum of the source neutrons and the cross section of Gd. Further reduction in the systematic errors due to the presence of Gd can be accomplished in two ways: First, redesigning the source moderator to have less flux at lower energies, and second, performing an additional measurement, alone or in combination with the fast-mode measurement, to determine the amount of Gd.

In addition, a Cd correction equivalent to the conventionally used “k_3,” but having a value appropriate for the PSD plastic collar, is developed and reported.

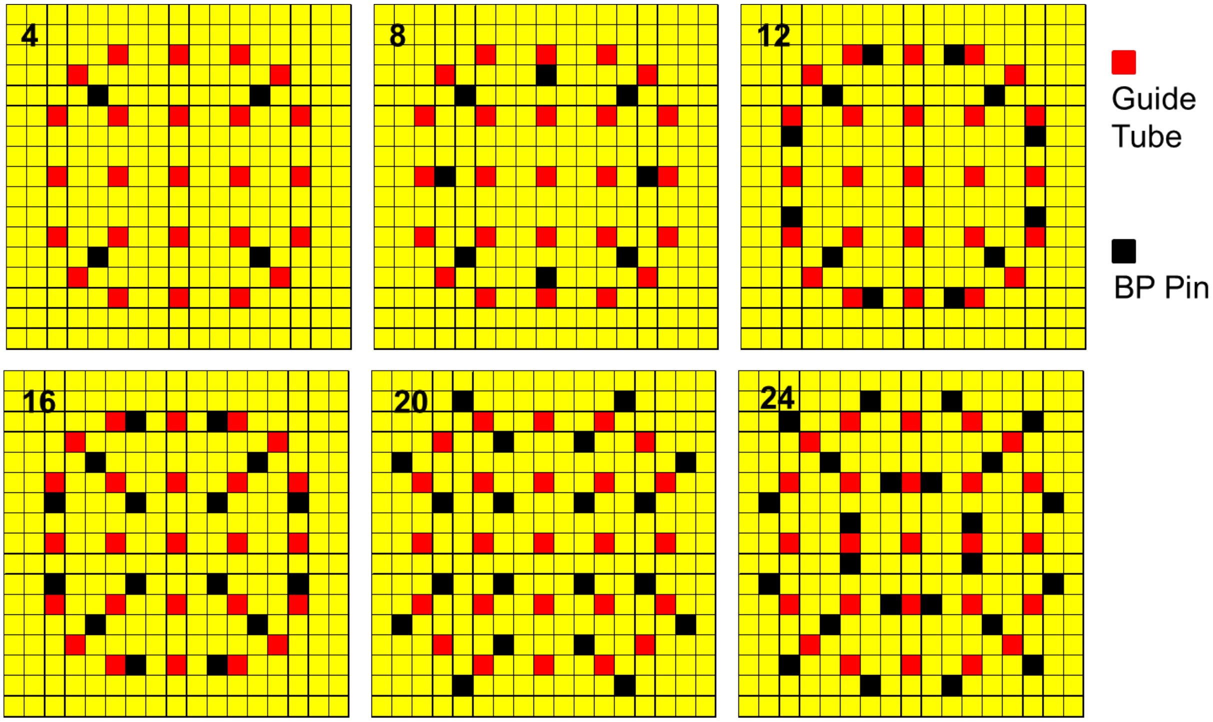

Fig. 19. The distribution of pins loaded with Gd in fuel assemblies as specified in the task plan to test sensitivity to burnable poisons.

3.4.1 Fast Mode Simulations of Configurations with Burnable Poisons

A summary of the simulated rates for configurations having burnable poisons measured in fast mode is shown in Table 13. Note that in fast mode the statistical error of the measurement of fission doubles is approximately 1% for all simulated measurements.

Table 13. Results of simulations for burnable poisons in fast mode, where *F* and *S* are the fission and scatter window count rates, respectively, and D_F is the inferred fission doubles rate.

Number of Gd Pins	Gd Density (%)	Source particles	$t_{equiv.}$ (s)	Neuts (s^{-1})	F (s^{-1})	S (s^{-1})	D_F (s^{-1})	ΔD_F (s^{-1})
0	0	3.57E+07	713.4	320.4	27.20	5.02	22.19	0.20
4	6	3.57E+07	714.1	316.9	26.75	4.80	21.95	0.20
8	6	3.57E+07	714.7	314.9	26.24	4.89	21.35	0.20
12	6	3.58E+07	715.1	312.6	25.94	4.83	21.10	0.20
16	6	3.58E+07	715.7	311.8	25.86	4.83	21.03	0.20
20	6	3.58E+07	716.2	308.9	25.43	4.78	20.65	0.19
24	6	3.58E+07	716.6	305.4	25.19	4.68	20.51	0.19
4	8	3.57E+07	714.1	317.5	26.51	4.88	21.62	0.20
8	8	3.57E+07	714.7	314.3	26.32	4.96	21.36	0.20
12	8	3.58E+07	715.4	310.9	25.44	5.01	20.43	0.19
16	8	3.58E+07	715.9	309.3	25.40	4.82	20.59	0.19
20	8	3.58E+07	716.6	307.3	24.90	4.80	20.09	0.19
24	8	3.59E+07	717.6	303.8	24.44	4.64	19.81	0.19
4	10	3.57E+07	714.1	318.3	26.98	4.95	22.03	0.20
8	10	3.58E+07	715.1	314.0	25.90	5.07	20.82	0.20
12	10	3.58E+07	715.7	311.4	25.84	4.92	20.91	0.20
16	10	3.58E+07	716.3	309.1	25.53	4.94	20.60	0.19
20	10	3.58E+07	716.9	306.5	25.05	4.52	20.52	0.19
24	10	3.59E+07	717.4	302.3	24.54	4.58	19.95	0.19

Each of the above cases was used, along with the calibration curve of Sect. 3.1.1, to calculate the analyzed linear density. The error in the analyzed linear density takes into account the statistical uncertainty of a 600-s measurement along with the uncertainty of the calibration curve. The declared linear densities and analyzed linear densities (along with uncertainties) are tabulated in Table 14. The total uncertainty reported takes into account an assumed 2% systematic error.

Table 14. Declared and analyzed linear densities for burnable poison fuel scenarios simulated in fast mode.

Number of Gd Pins	Gd Density (%)	Declared L_{235} (g/cm)	Analyzed L_{235} (g/cm)	600 s L_{235} Uncert (g/cm)	600 s Total Uncert (%)	Mass Defect
0	0	51.8	52.81	0.76	2.47%	1.9%
4	6	51.5	52.04	0.75	2.46%	1.0%
8	6	51.2	50.13	0.72	2.47%	−2.1%
12	6	50.9	49.37	0.71	2.47%	−3.0%
16	6	50.6	49.12	0.71	2.47%	−2.9%
20	6	50.3	47.96	0.69	2.47%	−4.7%
24	6	49.9	47.52	0.69	2.47%	−4.8%
4	8	51.5	51.00	0.74	2.47%	−1.0%
8	8	51.2	50.18	0.72	2.47%	−2.0%
12	8	50.9	47.28	0.69	2.47%	−7.1%
16	8	50.5	47.77	0.69	2.47%	−5.4%
20	8	50.2	46.25	0.67	2.47%	−7.9%
24	8	49.9	45.39	0.66	2.47%	−9.0%
4	10	51.5	52.29	0.75	2.47%	1.5%
8	10	51.2	48.49	0.70	2.47%	−5.3%
12	10	50.8	48.77	0.70	2.47%	−4.0%
16	10	50.5	47.80	0.69	2.47%	−5.4%
20	10	50.2	47.56	0.69	2.46%	−5.3%
24	10	49.8	45.83	0.66	2.47%	−8.0%

Prior to presenting the mass-defect results in graphical form, it is useful to consider the number of induced fissions in each assembly. The number of induced fissions was extracted from the simulation of each configuration and written as a fractional difference from the value expected for the given ^{235}U linear density. The fractional reduction data was then plotted as a function of the number of fuel pins containing Gd for each Gd weight fraction, and is shown in Fig. 20.

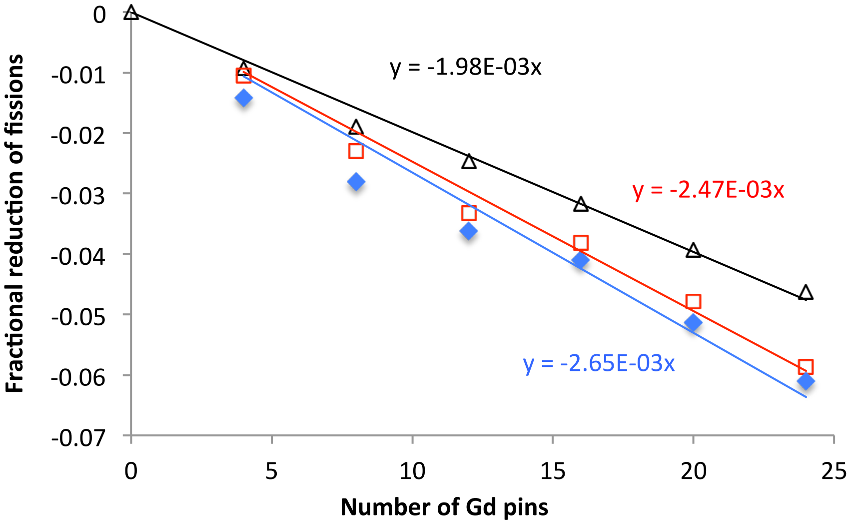

Fig. 20. The fractional reduction of the number fissions (in fast mode) as a function of the number of fuel pins containing Gd for (black) 6% Gd rods, (red) 8% Gd rods, and (blue) 10% Gd rods. The lines indicate the best-fit determination of the reduction of fissions per Gd rod.

The dependence of the number of induced fissions N_F on the linear densities of ^{235}U and Gd in fast mode is assumed to be of the following form:

$$N_F \sim \frac{aL_{235}}{1+bL_{235}}\left(\frac{1}{1+n\cdot 0.00359(1-e^{-0.138Gd})}\right),$$

where n is the number of Gd rods and the value Gd is the Gd weight fraction in percent. In words, the number of fissions due to the linear density of ^{235}U is reduced by the presence of Gd. The amount of that reduction depends on the number of Gd rods and the size of the correction for each rod, which in turn depends on the Gd loading. The slopes of the best-fit lines in Fig. 20 were used to extract the constants in the parenthetical second term that corrects for the presence of Gd. Note that the denominator of the second term is the correction factor commonly referred to as "k_3." However, the values of the numerical constants have been adjusted to be appropriate to the present configuration. The validity of this correction is shown in Fig. 21 where the induced fission data for the totality of burnable poison simulations has been plotted, in this case, with the fractional reduction of induced fissions as a function of the amount by which the correction factor k_3 exceeds one.

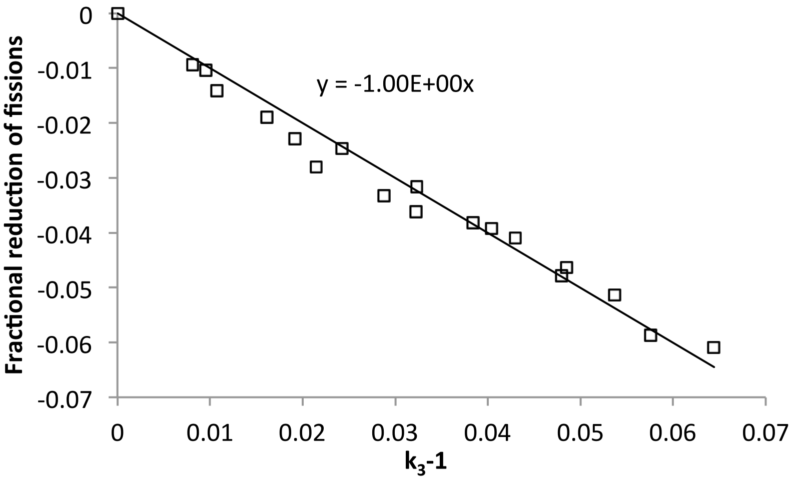

Fig. 21. The fractional reduction of induced fissions as a function of the correction factor $k_3 - 1$. The best fit to a straight line of slope −1 indicates that the correction works as desired.

Note that the value of the correction factor for the highest Gd loading and number of pins is 1.06, corresponding to a 5.7% deficit in the number of fissions compared to that expected without Gd. Now the data for the scenarios with differing Gd loadings can be combined on a single plot. This is done for the defects in ^{235}U linear density as a function of the amount by which the correction factor exceeds one, and is shown in Fig. 22. Here the slope of the best-fit line has a magnitude of slope greater than unity because the calculated defect in the mass depends on the slope of the calibration curve.

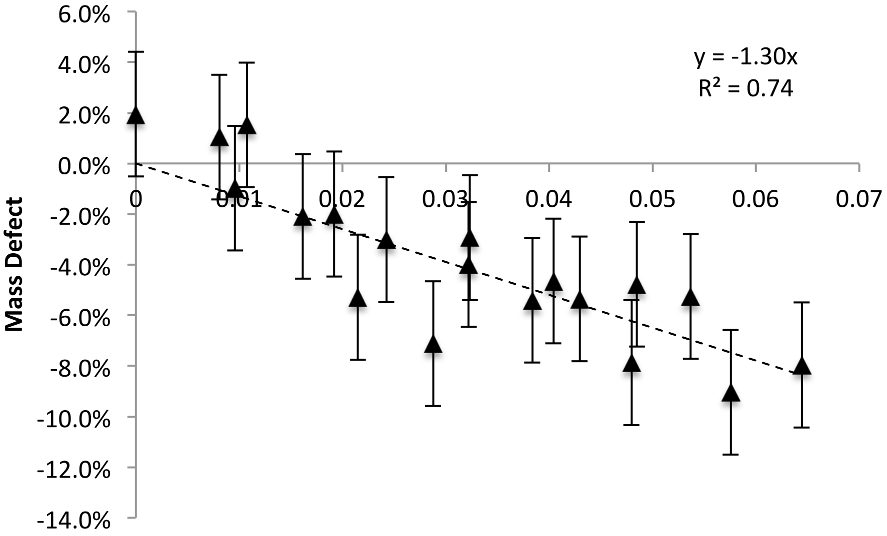

Fig. 22. The defect in linear density as a function of the correction factor factor $k_3 - 1$.

The reduction in the number of fissions due to the presence of Gd is responsible for the observed defect in linear density. Further reduction in the systematic errors due to the presence of Gd can be accomplished in two ways. First, further reduction in systematic error due to the presence of Gd could be accomplished through modification to the neutron spectrum that is interrogating the fuel. This modification can be accomplished to some degree by modification of the source moderator. Second, further reduction in systematic error can be accomplished by a second measurement that, alone or in combination with the fast-mode measurement, determines the amount of Gd.

3.4.2 Thermal Mode Simulations of Configurations with Burnable Poisons

A summary of the simulated rates for configurations having burnable poisons measured in thermal mode is shown in Table 15. Note that in thermal mode the statistical error of the measurement of fission doubles is approximately 0.35% for all simulated measurements.

Table 15. Results of simulations for burnable poisons in thermal mode, where F and S are the fission and scatter window count rates, respectively, and D_F is the inferred fission doubles rate.

Number of Gd Pins	Gd Density (%)	Source particles	$t_{equiv.}$ (s)	Neuts (s^{-1})	F (s^{-1})	S (s^{-1})	D_F (s^{-1})	ΔD_F (s^{-1})
0	0	2.33E+07	465.9	966617.0	262.33	45.44	216.89	0.77
4	6	2.36E+07	471.9	943018.0	249.91	43.66	206.25	0.75
8	6	2.39E+07	478.7	921084.0	240.38	41.84	198.54	0.73
12	6	2.43E+07	485.5	897955.0	228.74	40.16	188.58	0.71
16	6	2.46E+07	492.4	867134.0	216.58	38.37	178.21	0.68
20	6	2.49E+07	498.8	846624.0	208.01	36.48	171.53	0.67
24	6	1.34E+07	268.1	436379.0	197.17	34.86	162.31	0.88
4	8	2.36E+07	472.1	942259.0	251.66	43.98	207.68	0.75
8	8	2.39E+07	479.0	920621.0	238.84	41.84	197.00	0.73
12	8	2.43E+07	486.2	896033.0	229.21	40.39	188.82	0.71
16	8	2.46E+07	492.7	867499.0	216.48	38.72	177.76	0.68
20	8	2.50E+07	499.3	843497.0	204.67	36.50	168.16	0.66
24	8	2.53E+07	506.9	819130.0	195.84	34.53	161.31	0.64
4	10	2.36E+07	472.1	943342.0	250.51	43.33	207.18	0.75
8	10	2.40E+07	479.8	919063.0	238.27	42.36	195.90	0.73
12	10	2.43E+07	486.7	894337.0	226.51	40.06	186.45	0.70
16	10	2.47E+07	493.6	863412.0	214.04	37.59	176.45	0.68
20	10	2.50E+07	499.9	842768.0	205.72	36.47	169.26	0.66
24	10	2.51E+07	502.4	809738.0	194.72	34.50	160.22	0.64

Each of the above cases was used, along with the calibration curve of Sect. 3.1.2, to calculate the analyzed linear density. The error in the analyzed linear density takes into account the statistical uncertainty of a 600-s measurement along with the uncertainty of the calibration curve. The declared linear densities and analyzed linear densities (along with uncertainties) are tabulated in Table 16. The total uncertainty reported takes into account an assumed 2% systematic error.

Table 16. Declared and analyzed linear densities for burnable poison fuel scenarios simulated in thermal mode

Number of Gd Pins	Gd Density (%)	Declared L_{235} (g/cm)	Analyzed L_{235} (g/cm)	600 s L_{235} Uncert (g/cm)	600 s Total Uncert (%)	Mass Defect
0	0	51.8	51.61	0.68	2.39%	−0.4%
4	6	51.5	43.28	0.50	2.31%	−16.0%
8	6	51.2	38.39	0.41	2.27%	−25.0%
12	6	50.9	33.09	0.33	2.24%	−35.0%
16	6	50.6	28.52	0.27	2.21%	−43.6%
20	6	50.3	25.98	0.24	2.21%	−48.3%
24	6	49.9	22.90	0.21	2.20%	−54.1%
4	8	51.5	44.29	0.52	2.32%	−14.0%
8	8	51.2	37.50	0.40	2.26%	−26.8%
12	8	50.9	33.20	0.33	2.24%	−34.8%
16	8	50.5	28.35	0.27	2.21%	−43.9%
20	8	50.2	24.81	0.23	2.20%	−50.6%
24	8	49.9	22.59	0.21	2.20%	−54.7%
4	10	51.5	43.93	0.51	2.32%	−14.7%
8	10	51.2	36.88	0.39	2.26%	−28.0%
12	10	50.8	32.08	0.32	2.23%	−36.8%
16	10	50.5	27.83	0.26	2.21%	−44.9%
20	10	50.2	25.18	0.23	2.20%	−49.8%
24	10	49.8	22.26	0.20	2.20%	−55.3%

As before, it is useful to consider the number of induced fissions in each assembly. The number of induced fissions was extracted from the simulation of each configuration and written as a fractional difference from the value expected for the given ^{235}U linear density. The fractional-reduction data was then plotted as a function of the number of fuel pins containing Gd for each Gd weight fraction, and is shown in Fig. 23.

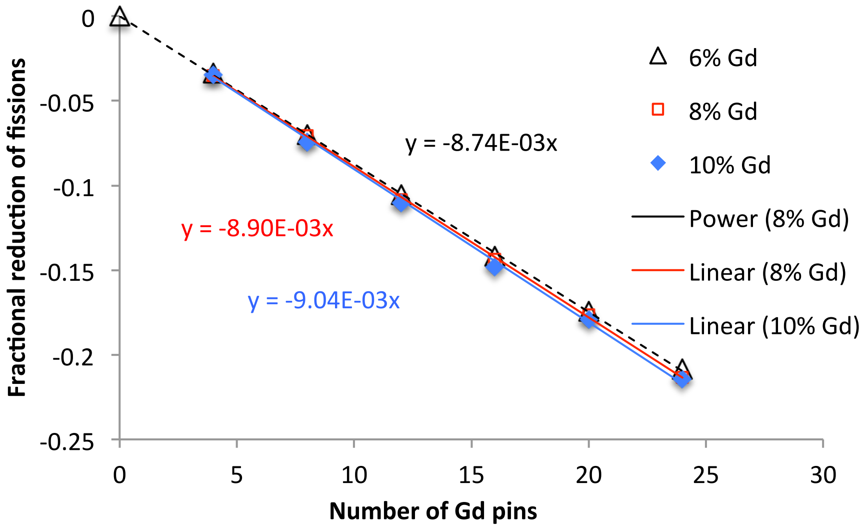

Fig. 23. The fractional reduction of the number fissions in thermal mode as a function of the number of fuel pins containing Gd for (black) 6% Gd rods, (red) 8% Gd rods, and (blue) 10% Gd rods. The lines indicate the best-fit determination of the reduction of fissions per Gd rod.

The same functional dependence of the number of induced fissions N_F on the linear densities of ^{235}U and Gd previously used for fast mode is again used for thermal mode. However, in thermal mode the constants determining the reduction in fissions per rod of Gd are different, and they are inferred from the best-fit slopes in Fig. 23. With the new constants extracted, the number of fissions is proportional to the following:

$$N_F \sim \frac{aL_{235}}{1+bL_{235}}\left(\frac{1}{1+n\cdot 0.00918(1-e^{-0.429Gd})}\right).$$

The validity of this correction is shown in Fig. 24 where the induced fission data for the totality of burnable poison simulations has been plotted, in this case with the fractional reduction of induced fissions as a function of the amount by which the correction factor k_3 exceeds one.

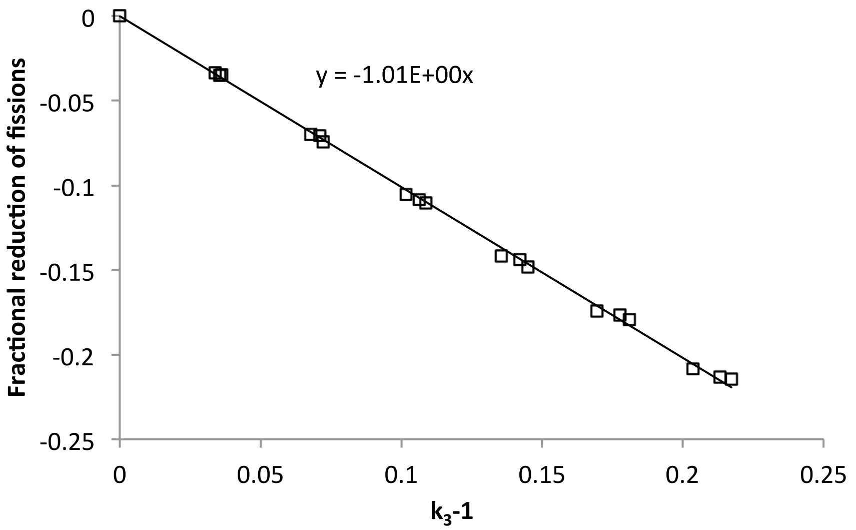

Fig. 24. The fractional reduction of induced fissions as a function of the correction factor $k_3 - 1$ for thermal-mode operation. The best fit to a straight line of slope -1 indicates that the correction works as desired.

As before, the data for the scenarios with differing Gd loadings can be combined on a single plot. This is done for the defects in ^{235}U linear density as a function of the amount by which the correction factor exceeds one, and is shown in Fig. 25. Here, a linear fit does not represent the data well because of the curvature of the calibration curve and the large magnitude of the correction effectively sampling different portions of the calibration curve.

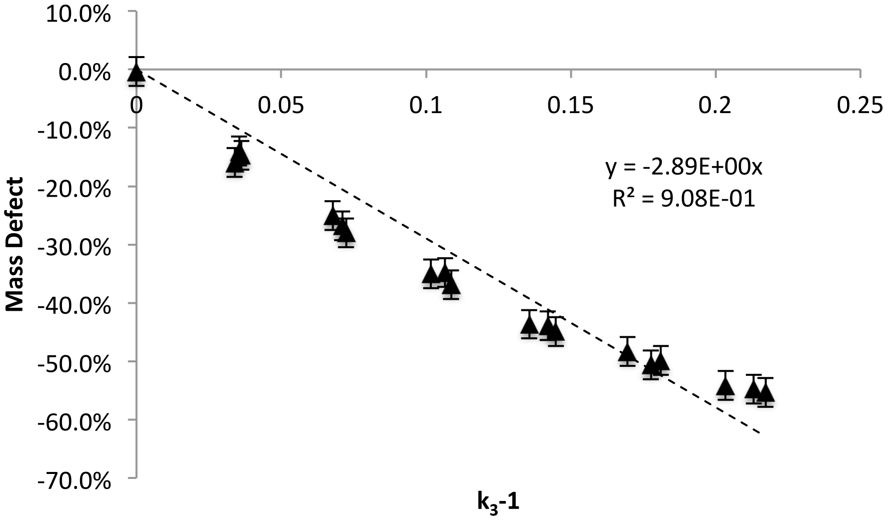

Fig. 25. The defect in linear density as a function of the correction factor factor $k_3 - 1$ for thermal-mode operation.

3.5 PASSIVE MEASUREMENT AND NET UNCERTAINTY IN 15 MINUTES

To this point, the results reported in the present work did not include the effects of the contribution of spontaneous fissions to the measurements. As a result, simulation of a passive measurement of spontaneous fissions from the ^{238}U component of fuel was performed for the 4.24% enriched (55 g/cm) calibration fuel. In the simulation, fissions originated in a one-meter length of the assembly centered on the PSD plastic collar. In the fuel, the linear density of the ^{238}U component corresponded to a linear density of 1242 g/cm or a fission rate of 840 fissions per second for a one-meter length. A 300-s measurement therefore corresponds to simulation of approximately 252,100 fissions. Then, the effect of the increase in statistical error due to performing a 600-s active measurement combined with a 300-s passive measurement could be evaluated.

3.5.1 Fast Mode Passive Measurement

A summary of the simulated rates for the passive measurement in fast mode is shown in Table 17. Note the statistical error associated with the passive measurement is higher than that of the active measurements because the rates are low.

Table 17. Results of simulations for a passive measurement in fast mode, where F and S are the fission and scatter window count rates, respectively, and D_F is the inferred fission doubles rate

Linear Density (g/cm)	Spon. Fissions	$t_{equiv.}$ (s)	Neuts (s^{-1})	F (s^{-1})	S (s^{-1})	D_F (s^{-1})	ΔD_F (s^{-1})	ΔD_F (s^{-1}) 300 s	$\Delta D_F/D_F$ (%) 300 s
55	3.00E+06	3569.2	92.6	7.44	1.78	7.77	0.05	0.18	2.36%

These passive results can be combined with the active simulations to infer the total active doubles rate and its associated statistical error, and therefore, the net rates and the corresponding statistical error. These are reported in Table 18. Note that the error in the net induced doubles rate is less than 2%.

Table 18. The statistical errors for the active and passive measurements as well as the net active measurement in fast mode

Meas. Type	Time (s)	D_F (s^{-1})	ΔD_F (s^{-1})	$\Delta D_F/D_F$ (%)
Active	600	31.01	0.26	0.97%
Passive	300	7.77	0.18	2.36%
Net	-	23.24	0.32	1.37%

3.5.2 Thermal Mode Passive Measurement

A summary of the simulated rates for the passive measurement in thermal mode is shown in Table 19. Unlike the active measurements, the passive measurements in thermal mode have similar statistical errors to those in fast mode since the majority of the fissions are the spontaneous fissions themselves rather than induced fissions from neutrons that have returned to the assembly after moderation in the detector.

Table 19. Results of simulations for a passive measurement in thermal mode, where F and S are the fission and scatter window count rates, respectively, and D_F is the inferred fission doubles rate.

Linear Density (g/cm)	Spon. Fissions	$t_{equiv.}$ (s)	Neuts (s^{-1})	F (s^{-1})	S (s^{-1})	D_F (s^{-1})	ΔD_F (s^{-1})	ΔD_F (s^{-1}) 300 s	$\Delta D_F/D_F$ (%) 300 s
55	3.00E+06	3569.2	109.5	9.66	2.30	10.09	0.06	0.21	2.07%

Again, these passive thermal mode results can be combined with the active simulations to infer the total active doubles rate and its associated statistical error, and therefore the net rates and the corresponding statistical error. These are reported in Table 20. Note that because the induced doubles rate is much larger than the passive doubles rate, the error in the net induced doubles differs only slightly from that of a background-free measurement.

Table 20. The statistical errors for the active and passive measurements as well as the net active measurement in thermal mode.

Meas. Type	Time (s)	D_F (s^{-1})	ΔD_F (s^{-1})	$\Delta D_F/D_F$ (%)
Active	600	229.92	0.70	0.31%
Passive	300	10.09	0.21	2.07%
Net	-	219.83	0.73	0.33%

3.6 NOTIONAL DESIGN AND DISCUSSION

In addition to the performance limitations of a notional collar due to the physics constraints of the materials used for detection, there are many additional considerations for a practical device. For instance, the size and portability, safety, robustness, and cost all factor into a practical device. The evaluation of these criteria can be made both for existing PSD plastic detectors and for potential future implementations based on a compact and rugged SiPM readout. However, a worst case can be based on the present detectors. A schematic diagram of a notional PSD plastic collar based on existing detectors is shown in the plan view in Fig. 26.

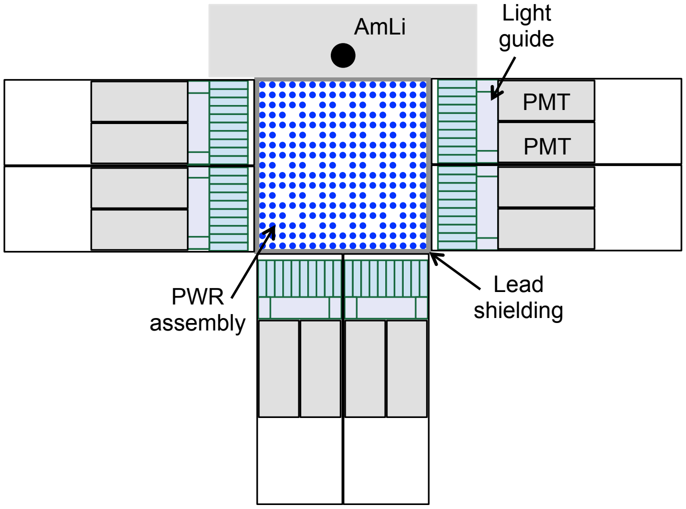

Fig. 26. Notional design of a PSD plastic collar (in plan view) using existing segmented PSD plastic detectors.

For instance, a total of twelve segmented detectors could make up a collar, with a module consisting of four detectors on each of three sides. If it is desirable to increase sensitivity on the side opposite the source, the module on that side could be made up of six detectors. Each four-detector module would measure approximately 22 × 22 × 40 cm, and each module would assemble on a measurement cart with the long direction facing perpendicular to the fuel. Using the weight and cost of the present detectors, a four-detector module would weigh 16 kg (with 0.6 cm lead shielding only facing the fuel) and would cost approximately $50,000, including the cost of the 16-channel digitizer to read out the detector signals. Three such detector panels would be required to instrument the collar and would cost $150,000. Including the cart and source moderator, the total cost would be approximately $160,000 (excluding the ^{241}Am/Li source). This overall cost is similar to that of the UNCL, which is $142,000 (excluding the ^{241}Am/Li source and shift register). The individual modules would need to be connected via an ethernet cable and a fast timing cable. Note that with the detectors arranged in this manner, the backs of the detectors are susceptible to gamma rays from neighboring fuel assemblies. It is likely that the backs of the detectors would require lead (or other high-Z) shielding, which would add significantly to the weight with the present size of detectors. Development to allow a compact PMT or SiPM readout could dramatically reduce the size of the detectors to approximately one-third their present length, or about 12 cm. This reduction in size would bring a corresponding reduction in weight.

The PSD plastic collar would require gain calibration using a ^{137}Cs source. This same source, using inter-detector scattering, can be used to line up detector times. A ^{241}Am/Be source can be used to measure the distribution of time excesses for scattered neutrons and can also be used for calibration of the pulse shape discrimination.

The PSD plastic has no inherent safety risks associated with it. The detectors, in their present state, are sufficiently robust for shipment, but not robust against, e.g., dropping on the floor.

4. SUMMARY

The potential performance of a notional active coincidence collar for assaying uranium fuel based on segmented detectors constructed from fast organic scintillator was investigated in simulation. While the study was motivated by the availability of the new “PSD plastic” scintillator with pulse shape discrimination capability, the composition and density of organic scintillators are sufficiently similar that the results of this study are pertinent to the use of other commercially available organic scintillators.

In confirmation of expectations, the fast time scale of detection in the scintillator eliminates statistical errors due to accidental coincidences that limit the performance of the UNCL, particularly in fast mode. Furthermore, the position and timing resolution of segmented detectors allow true neutron-neutron coincidences to be distinguished from inter-detector scattering. This identification of scatter and true doubles via relative time and distance appears to be robust, and it enables a detector solution using close-packed segmented detectors that has higher efficiency and better accuracy than the corresponding solution having inter-detector shielding. Interestingly, relatively small monolithic detectors, if appropriately used, can obtain most of the benefit. However, doing so requires independently knowing (or calculating) the shape of the “excess time” distribution for fission neutrons rather than inferring it from measurement.

Despite the large size of individual detectors, coincidence summing was not a significant source of systematic error. Although it lowered the detected doubles rate by 25%, it increased the relative error of measurements by only 5%. A much more significant effect was due to having the source, and therefore most of the induced fission, on one side of the fuel. Although not yet quantified, placing more detectors on the side opposite the source would counteract this effect.

The performance of the notional simulated coincidence collar was evaluated for assaying a variety of fresh fuels, including some containing burnable poisons and partial defects. In these simulations, particular attention was paid to the investigation of “fast mode” measurements, where a Cd liner eliminates the thermalized neutron flux from the source and detector moderators that is most sensitive to the presence of burnable poisons that are ubiquitous in modern nuclear fuels. The simulations indicate that the predicted precision of fast mode measurements is similar to what can be achieved by the present UNCL in thermal mode. For example, the statistical accuracy of a ten-minute measurement of fission coincidences collected in “fast mode” will be approximately 1% for most fuels of interest, yielding a ~1.4% error after subtraction of a five-minute measurement of the spontaneous fissions from ^{238}U in the fuel, a ~2% error in analyzed linear density after accounting for the slope of the calibration curve, and a ~2.9% total error after addition of an assumed systematic error of 2%. Moreover, the simulations indicate that the accuracy of assay where burnable poisons are present is limited by the reduction in induced fissions caused by the presence of Gd. This reduction in induced fissions is simply a consequence of the energy spectrum of the source neutrons and the cross section of Gd. Further reduction in the systematic errors due to the presence of Gd can be accomplished in two ways: first, redesigning the source moderator to have less flux at lower energies, and second, performing an additional measurement, alone or in combination with the fast-mode measurement, to determine the amount of Gd.

Although the present results are promising, the present work has also identified avenues of investigation that would be beneficial. For instance, it would be desirable to simulate nearby uncorrelated sources to demonstrate that they do not contribute to the correlated doubles. Likewise, it would be desirable to vary the number of detectors on the side opposite the interrogation source to even out the response as much as possible. Moreover, changes to the source moderator that made the assay less sensitive to the presence of Gd would also be of interest, as would measurements that could determine the amount of Gd. One potential way to measure the amount of Gd could be via a thermal-neutron transmission measurement through the fuel assembly. This could be accomplished via a Cd shutter on the source moderator, and the existing segmented detectors already incorporate thermal phosphor on the front face for the detection of thermal neutrons. Then, the number of induced fissions combined with the transmission of thermal neutrons could together determine both the Cd and fissile content of the assembly. Another potential way to determine the Gd content could be by performing the assay with a pulsed source such as a deuterium-deuterium neutron generator. In this case, an assay measurement would correspond to both the magnitude of the induced fission signal and the time dependence of the die-away measurement. The combination may be able to determine both the Gd and fissile content.

Last of all, it is worth mentioning that the size of the present detectors can be reduced to approximately one-third the present size by use of either compact PMTs or an array of SiPMs. This reduction in size would realize a corresponding reduction in weight and help to make such a detector readily deployable.

REFERENCES

[1] H. O. Menlove, *Description and Performance Characteristics for the Neutron Coincidence Collar for the Verification of Reactor Fuel Assemblies*, LA-8939-MS (ISPO-142), Los Alamos National Laboratory, August 1981.

[2] H. O. Menlove et al., *Neutron Collar Calibration and Evaluation for Assay of LWR Fuel Assemblies Containing Burnable Neutron Absorbers*, LA-11965-MS (ISPO-323), Los Alamos National Laboratory, November 1990.

[3] N. Zaitseva, A. Glenn, L. Carman, and S. Payne, "Scintillation properties of solution-grown trans-stilbene single crystals," *Nuclear Instruments and Methods in Physics Research, Section A, Accelerators, Spectrometers, Detectors and Associated Equipment*, 789, 2015 p. 8.

[4] Zaitseva N., B. L. Rupert, I. Pawelczak, A. Glenn, H. P. Martinez, L. Carman, M. Faust, N. Cherepy, and S. Payne, "Plastic Scintillators with Efficient Neutron/Gamma Pulse Shape Discrimination," *Nuclear Instruments and Methods in Physics Research, Section A, Accelerators, Spectrometers, Detectors and Associated Equipment*, 668, 2012, p. 88-93.

[5] P. A. Hausladen, R. D. McElroy, and J. Newby, *Active-Well Counting Using New 'PSD Plastic' Detectors*, ORNL/TM-2015/651, Oak Ridge National Laboratory, 2015.

[6] J. Verbeke, C. Hagmann, D. Wright, Simulation of Neutron and Gamma Ray Emission from Fission and Photofission, UCRL-AR-228518, Lawrence Livermore National Laboratory, 2010.